Chapter 4

Decomposition of Superimposed TDR Reflections

4.1 Introduction

The experience with the TDR-response based identification of subscriber loops in the previous chapter indicates the need for an algorithm that can decompose a linear combination of closely spaced, strongly overlapping pulses of similar shape. This chapter presents two variations of the so called method of direction estimation (MODE) algorithm [21], [22], which employs advanced signal processing techniques to resolve overlapping pulses. The MODE algorithm is a type of eigenanalysis method [23] — also known as subspace methods [24] — and is closely related to such algorithms as Pisarenko's, MUSIC, and ESPRIT [23], [24]. The two MODE-based algorithms used are the MODE algorithm with the weighted Fourier transform and relaxation (WRELAX) algorithm (referred to hereafter as the MODE-WRELAX algorithm) [25] and the MODE-type algorithm [26].

The first part of the chapter covers the analysis, implementation, and application of the MODE-WRELAX algorithm, which was used first in the course of this research. The following sections constitute the first part:

- Problem formulation (Section 4.2),
- MODE-WRELAX algorithm (Section 4.3), and
- Application of MODE-WRELAX algorithm in TDR reflection decomposition (Section 4.4).

The performance of the MODE-WRELAX algorithm is limited when the overlapping TDR reflections are dissimilar due to the dispersive behavior of the TP. To accommodate the dispersion effect of TP, the MODE-type algorithm was investigated next. The second half of the chapter is devoted to studying the latter algorithm and its application to TDR reflection separation:

- Problem reformulation — TP analysis for dispersion modeling (Section 4.5),
- MODE-type algorithm (Section 4.6),

- Application of MODE-type algorithm in TDR reflection decomposition (Section 4.7).

The compatibility of the signal model, used in the MODE-type algorithm, with general TDR reflections is verified in Section 4.5.1.

4.2 Formulation of Problem

The MODE-WRELAX algorithm resolves closely spaced overlapping pulses described in the continuous-time domain by:

$$y(t) = \sum_{l=1}^{L} a_l s(t - \tau_l) \tag{4-1}$$

There are L pulses, defined by the known reference signal $s(t)$, and the corresponding scaling factors a_l and time-delays τ_l. The sampled version of $y(t)$ can be written as

$$y(nT_s) = \sum_{l=1}^{L} a_l s(nT_s - \tau_l) \tag{4-2}$$

where T_s is the sampling period. Furthermore, assuming time-domain aliasing can be ignored, the N-point DFT Y_k of the above equation can be expressed as

$$Y_k = S_k \sum_{l=1}^{L} a_l e^{j\omega_l k} \tag{4-3}$$

with

$$\omega_l = -\frac{2\pi\tau_l}{NT_s}. \tag{4-4}$$

Note that (4-3) can also be obtained by sampling the continuous-time Fourier transform of (4-1). Equation (4-3) can be rewritten in matrix form as follows.

$$\mathbf{y} = \mathbf{SEa} \tag{4-5}$$

where

$$\mathbf{y} = \left[Y_{-N/2} \quad Y_{-N/2+1} \quad \cdots \quad Y_{N/2-1} \right]^T \tag{4-6}$$

$$\mathbf{S} = diag\ \left\{ S_{-N/2}, S_{-N/2+1}, \cdots, S_{N/2-1} \right\} \tag{4-7}$$

$$\mathbf{a} = \left[a_1 \quad a_2 \quad \cdots \quad a_L \right]^T \tag{4-8}$$

and

$$\mathbf{E} = \left[\mathbf{e}(\omega_1) \quad \mathbf{e}(\omega_2) \quad \cdots \quad \mathbf{e}(\omega_L) \right] \tag{4-9}$$

with

$$\mathbf{e}(\omega_l) = \left[e^{j\omega_l(-N/2)} \quad e^{j\omega_l(-N/2+1)} \quad \cdots \quad e^{j\omega_l(N/2-1)} \right]^T \tag{4-10}$$

The operator $(\cdot)^T$ is the matrix transpose operator.

It is important to note that the algorithm does not require all of the DFT points. Subsets of the DFT samples can be masked (the information is not considered at all) or weighted (to express varying degrees of confidence in measurements at different frequencies) before being applied in the MODE-WRELAX routine.

4.3 MODE-WRELAX Algorithm

The MODE-WRELAX algorithm is a two-fold approach to resolving closely spaced overlapping signals of the same shape. Both stages, namely the MODE and the WRELAX algorithm, are approximations of the maximum likelihood method [23], [24], [27], [22]. Both algorithms aim at obtaining an optimal solution by minimizing the criterion $C_1(\mathbf{a}, \boldsymbol{\omega})$

$$\arg \min_{\mathbf{a},\boldsymbol{\omega}} C_1(\mathbf{a}, \boldsymbol{\omega}) = \arg \min_{\mathbf{a},\boldsymbol{\omega}} \left\| \mathbf{y} - \mathbf{SEa} \right\|^2 \tag{4-11}$$

where $\mathbf{a} = \begin{bmatrix} a_1 & a_2 & \cdots & a_L \end{bmatrix}^T$ and $\boldsymbol{\omega} = \begin{bmatrix} \omega_1 & \omega_2 & \cdots & \omega_L \end{bmatrix}^T$. For fixed $\boldsymbol{\omega}$, we can minimize the above expression with respect to **a** by solving a nonlinear least squares problem, with as formal solution

$$\mathbf{a} = \left(\mathbf{E}^H \mathbf{S}^H \mathbf{S}\mathbf{E}\right)^{-1} \mathbf{E}^H \mathbf{S}^H \mathbf{y} \tag{4-12}$$

where $(\cdot)^H$ is the Hermitian transpose (conjugate transpose) operator. Therefore, if we can find the solution for $\boldsymbol{\omega}$, we can find the corresponding solution for **a,** from (4-12), in straightforward fashion. The above facilitates turning the criterion in (4-11) into one where only $\boldsymbol{\omega}$ is unknown. Substituting (4-12) into (4-11) yields

$$\begin{aligned} C_1 &= \left\| \mathbf{y} - \mathbf{S}\mathbf{E}\left(\mathbf{E}^H \mathbf{S}^H \mathbf{S}\mathbf{E}\right)^{-1} \mathbf{E}^H \mathbf{S}^H \mathbf{y} \right\|^2 \\ &= \left[\mathbf{y} - \mathbf{S}\mathbf{E}\left(\mathbf{E}^H \mathbf{S}^H \mathbf{S}\mathbf{E}\right)^{-1} \mathbf{E}^H \mathbf{S}^H \mathbf{y}\right]^H \left[\mathbf{y} - \mathbf{S}\mathbf{E}\left(\mathbf{E}^H \mathbf{S}^H \mathbf{S}\mathbf{E}\right)^{-1} \mathbf{E}^H \mathbf{S}^H \mathbf{y}\right] \end{aligned} \tag{4-13}$$

After further simplification, the criterion becomes

$$C_1 = \mathbf{y}^H \left[\mathbf{I} - \overline{\mathbf{E}}\left(\overline{\mathbf{E}}^H \overline{\mathbf{E}}\right)^{-1} \overline{\mathbf{E}}^H\right] \mathbf{y} \tag{4-14}$$

where $\overline{\mathbf{E}} = \mathbf{S}\mathbf{E}$. Notice that

$$\mathbf{P}_{\overline{\mathbf{E}}} = \overline{\mathbf{E}}\left(\overline{\mathbf{E}}^H \overline{\mathbf{E}}\right)^{-1} \overline{\mathbf{E}}^H \tag{4-15}$$

and

$$\mathbf{P}_{\overline{\mathbf{E}}}^{\perp} = \mathbf{I} - \overline{\mathbf{E}}\left(\overline{\mathbf{E}}^H \overline{\mathbf{E}}\right)^{-1} \overline{\mathbf{E}}^H \tag{4-16}$$

are projectors onto $\mathrm{sp}\{\overline{\mathbf{E}}\}$ (the span of the columns of $\overline{\mathbf{E}}$) and onto its orthogonal complement, respectively.

While the objective of both the MODE and WRELAX algorithms is to minimize the criterion in (4-11), the algorithms approach the problem differently. The MODE algorithm, based on an eigenanalysis technique, determines the optimal solution such that it minimizes the projection of $\mathbf{y}$ onto $\mathbf{P}_{\overline{\mathbf{E}}}^{\perp}$:

$$\arg\min_{\mathbf{a},\boldsymbol{\omega}}\{C_{MODE}\} = \arg\min_{\mathbf{a},\boldsymbol{\omega}}\{\mathbf{y}^H \mathbf{P}_{\overline{\mathbf{E}}}^{\perp} \mathbf{y}\} \tag{4-17}$$

The WRELAX algorithm, on the other hand, maximizes the projection of $\mathbf{y}$ onto $\mathbf{P}_{\overline{\mathbf{E}}}$ through a series of iterations:

$$\arg\max_{\mathbf{a},\boldsymbol{\omega}}\{C_{WRELAX}\} = \arg\max_{\mathbf{a},\boldsymbol{\omega}}\{\mathbf{y}^H \mathbf{P}_{\overline{\mathbf{E}}} \mathbf{y}\} \tag{4-18}$$

The MODE-WRELAX algorithm combines the efforts of both the MODE and WRELAX algorithms, aiming for improved accuracy and efficiency. The result of the MODE algorithm, the first stage, is expected to provide a good initialization for the WRELAX stage, which attempts to improve the MODE estimates.

4.3.1 MODE Algorithm

To proceed with the minimization defined in (4-17), we aim to find a matrix $\overline{\mathbf{B}}$ such that

$$\mathbf{P}_{\overline{\mathbf{E}}}^{\perp} = \mathbf{I} - \overline{\mathbf{E}}\left(\overline{\mathbf{E}}^H \overline{\mathbf{E}}\right)^{-1} \overline{\mathbf{E}}^H = \overline{\mathbf{B}}\left(\overline{\mathbf{B}}^H \overline{\mathbf{B}}\right)^{-1} \overline{\mathbf{B}}^H \tag{4-19}$$

or

$$\overline{\mathbf{B}}\left(\overline{\mathbf{B}}^H \overline{\mathbf{B}}\right)^{-1} \overline{\mathbf{B}}^H + \overline{\mathbf{E}}\left(\overline{\mathbf{E}}^H \overline{\mathbf{E}}\right)^{-1} \overline{\mathbf{E}}^H = \mathbf{I} \tag{4-20}$$

To fulfill such a relationship between $\overline{\mathbf{B}}$ and $\overline{\mathbf{E}}$, $\overline{\mathbf{B}}$ must be a full-rank matrix of dimension $N \times (N - L)$, and the following must hold [28]:

$$\overline{\mathbf{B}}^H \overline{\mathbf{E}} = \mathbf{0} \tag{4-21}$$

We can interpret (4-21) as a solution to a polynomial $B(z)$ with its roots at $e^{j\omega_l}$ for $l = 1 : L$, i.e.

$$B(z) = \sum_{k=0}^{L} b_k z^k = b_L \prod_{l=1}^{L} \left(z - e^{j\omega_l}\right) \tag{4-22}$$

Consequently the following is valid.

$$B(z)\Big|_{z=e^{j\omega_l}} = \sum_{k=0}^{L} b_k e^{j\omega_l k} = 0 \quad \forall \quad l = 1:L \tag{4-23}$$

Furthermore, multiplying (4-23) left and right by $e^{j\omega_l n}$ we have the following:

$$e^{j\omega_l n} \sum_k b_k e^{j\omega_l k} = 0 \tag{4-24}$$

for all $l = 1:L$, assuming $b_k = 0$ for $k < 0$ and for $k > L$, and any arbitrary n. Writing (4-24) for $n = -\frac{N}{2}$, in matrix form, using $\mathbf{E}$, yields

$$\begin{bmatrix} b_0 & \cdots & b_L & 0 & \cdots & 0 \end{bmatrix} \mathbf{E} = \mathbf{0} \tag{4-25}$$

Writing (4-24) for $n = -\frac{N}{2} + 1$ produces

$$\begin{bmatrix} 0 & b_0 & \cdots & b_L & 0 & \cdots & 0 \end{bmatrix} \mathbf{E} = \mathbf{0} \tag{4-26}$$

Equations (4-24) and (4-26) begin to look like (4-21); the vector $\begin{bmatrix} b_0 & \cdots & b_L & 0 & \cdots & 0 \end{bmatrix}$ can be used to define the Hermitian transpose of a full-rank $N \times (N-L)$ matrix. The matrix $\mathbf{B}^{\mathrm{H}}$ can in fact be defined as a Toeplitz matrix with the above vector as its first row:

$$\mathbf{B}^H = \begin{bmatrix} b_0 & \cdots & b_L & & & 0 \\ & b_0 & \cdots & b_L & & \\ & & \ddots & & \ddots & \\ 0 & & & b_0 & \cdots & b_L \end{bmatrix}_{(N-L)\times N} \tag{4-27}$$

and

$$\mathbf{B}^{H}\mathbf{E} = \mathbf{0} \tag{4-28}$$

From (4-21) and (4-28) — with some matrix algebra — we can conclude

$$\overline{\mathbf{B}} = \mathbf{S}^{-H}\mathbf{B} \tag{4-29}$$

We can substitute for the matrix $\overline{\mathbf{B}}$ in the C_{MODE} criterion of (4-17)

$$\begin{aligned} C_{MODE} &= \mathbf{y}^{H}\mathbf{P}_{\overline{\mathbf{E}}}^{\perp}\mathbf{y} \\ &= \mathbf{y}^{H}\left(\overline{\mathbf{B}}\left(\overline{\mathbf{B}}^{H}\overline{\mathbf{B}}\right)^{-1}\overline{\mathbf{B}}^{H}\right)\mathbf{y} \end{aligned} \tag{4-30}$$

Since the projection matrix $\mathbf{P}_{\overline{\mathbf{E}}}^{\perp}$ is both Hermitian and idempotent, (4-30) can be simplified to

$$C_{MODE} = \left\|\overline{\mathbf{B}}\left(\overline{\mathbf{B}}^{H}\overline{\mathbf{B}}\right)^{-1}\overline{\mathbf{B}}^{H}\mathbf{y}\right\|^{2} \tag{4-31}$$

Rewriting $\overline{\mathbf{B}}^{H}\mathbf{y}$ as $\overline{\mathbf{Y}}\mathbf{b}$, defining $\mathbf{b} = \begin{bmatrix} b_L & b_{L-1} & \cdots & b_0 \end{bmatrix}^{T}$, and

$$\overline{\mathbf{Y}} = \begin{bmatrix} \overline{Y}_{-N/2+L} & \overline{Y}_{-N/2+L-1} & \cdots & \overline{Y}_{-N/2} \\ \overline{Y}_{-N/2+L+1} & \overline{Y}_{-N/2+L} & \cdots & \overline{Y}_{-N/2+1} \\ \vdots & \vdots & \ddots & \vdots \\ \overline{Y}_{N/2-1} & \overline{Y}_{N/2-2} & \cdots & \overline{Y}_{N/2-L-1} \end{bmatrix} \tag{4-32}$$

with $\overline{Y}_k = \dfrac{Y_k}{S_k}$ due to the diagonal nature of **S**. Consequently, (4-31) can be rewritten as

$$C_{MODE} = \left\|\overline{\mathbf{B}}\left(\overline{\mathbf{B}}^{H}\overline{\mathbf{B}}\right)^{-1}\overline{\mathbf{Y}}\mathbf{b}\right\|^{2} \tag{4-33}$$

Simplifying (4-33) further yields

$$C_{MODE} = \mathbf{b}^{H}\overline{\mathbf{Y}}^{H}\left(\overline{\mathbf{B}}^{H}\overline{\mathbf{B}}\right)^{-H}\overline{\mathbf{Y}}\mathbf{b} \tag{4-34}$$

Let

$$\mathbf{\Omega} = \overline{\mathbf{Y}}^H \left(\overline{\mathbf{B}}^H \overline{\mathbf{B}} \right)^{-H} \overline{\mathbf{Y}} \tag{4-35}$$

Then (4-34) becomes

$$C_{MODE} = \mathbf{b}^H \mathbf{\Omega} \mathbf{b} \tag{4-36}$$

To avoid the obvious minimizing solution, $\mathbf{b} = \mathbf{0}$, assume that $\mathbf{b}$ has non-zero norm. Then we can rewrite the minimization criterion as

$$C_{MODE} = \frac{\mathbf{b}^H \mathbf{\Omega} \mathbf{b}}{\mathbf{b}^H \mathbf{b}} \tag{4-37}$$

Let

$$\mathbf{\Lambda} = \mathrm{diag}\{\lambda_1, \lambda_2, \cdots, \lambda_{L+1}\} \tag{4-38}$$

where λ_i is an eigenvalue of $\mathbf{\Omega}$. Also, define a matrix $\mathbf{V}$, whose columns consist of the unitary eigenvectors of $\mathbf{\Omega}$, such that

$$\mathbf{\Omega V} = \mathbf{V \Lambda} \tag{4-39}$$

Assume $\mathbf{b}$ to be expressed in terms of the eigenvector basis

$$\mathbf{b} = \mathbf{Vc} \tag{4-40}$$

where $\mathbf{c}$ is some arbitrary vector of length L+1. Substituting (4-30) into (4-37) yields

$$C_{MODE} = \frac{\mathbf{c}^H \mathbf{V}^H \mathbf{\Omega V c}}{\mathbf{c}^H \mathbf{V}^H \mathbf{V c}} \tag{4-41}$$

Note that since $\mathbf{V}$ is unitary, $\mathbf{V}^H \mathbf{V} = \mathbf{I}$. Incorporating this property and substituting (4-39) into (4-41) results in

$$C_{MODE} = \frac{\mathbf{c}^H \mathbf{\Lambda c}}{\mathbf{c}^H \mathbf{c}} \tag{4-42}$$

To minimize the above expression, we can select the vector **c** such that it has zero elements everywhere except for the element corresponding to the minimum eigenvalue in Λ, which equals one. Note that selecting such a **c** translates into choosing for **b** in (4-37) the eigenvector corresponding to the minimum eigenvalue, using (4-30).

Once **b** is determined, **ω** can be derived by finding the roots of the polynomial $B(z)$, with its coefficients given in **b**, as defined in (4-22). Moreover, we can obtain the gain vector **a** by solving (4-12) and the delay vector $\boldsymbol{\tau} = [\tau_1 \quad \tau_2 \quad \cdots \quad \tau_L]$ from

$$\boldsymbol{\tau} = \frac{-\boldsymbol{\omega} N T_s}{2\pi} \tag{4-43}$$

To implement the MODE algorithm, the $\mathbf{\Omega}$ in (4-24) must be defined, given dataset **y** and **s** as well as an arbitrary polynomial $B_o(z)$ as the initial guess for $B(z)$. We have defined $B_o(z)$ to have its roots evenly spaced on the unit circle.

4.3.2 WRELAX Algorithm

Maximizing the criterion defined in (4-18) is a highly nonlinear optimization problem and it is very difficult to find the global minimum. Instead, the WRELAX algorithm reformulates the problem by decomposing Y_k into a sum of the DFTs of individual pulses.

$$Y_k = \sum_{l=1}^{L} Y_{l,k} \tag{4-44}$$

where

$$Y_{l,k} = a_l S_k e^{j\omega_l k} \tag{4-45}$$

The equations can be expressed in matrix form

$$\mathbf{y} = \sum_{l=1}^{L} \mathbf{y}_l \tag{4-46}$$

$$\mathbf{y}_l = a_l \mathbf{Se}(\omega_l) \tag{4-47}$$

where

$$\mathbf{y}_l = \begin{bmatrix} Y_{l,-N/2} & Y_{l,-N/2+1} & \cdots & Y_{l,N/2-1} \end{bmatrix}^T \tag{4-48}$$

From (4-46) and (4-47), we can define $\mathbf{y}_m$ for $m \in 1{:}L$ as

$$\mathbf{y}_m = \mathbf{y} - \sum_{l=1, l\neq m}^{L} a_l \mathbf{Se}(\omega_l) \tag{4-49}$$

The nonlinear least squares criterion defined in (4-11) is then simplified to contain a single pulse (assuming all others to be known).

$$C_2(a_m, \omega_m) = \left\| \mathbf{y}_m - a_m \mathbf{Se}(\omega_m) \right\|^2 \tag{4-50}$$

For fixed ω_m, we can minimize the above expression with respect to a_m by solving a nonlinear least squares problem, with solution

$$a_m = \left(\mathbf{e}(\omega_m)^H \mathbf{S}^H \mathbf{Se}(\omega_m) \right)^{-1} \mathbf{e}(\omega_m)^H \mathbf{S}^H \mathbf{y}_m \tag{4-51}$$

Since $\mathbf{e}(\omega_m)$ is always on the unit circle, the expression can be simplified to

$$a_m = \frac{\mathbf{e}^H(\omega_m)\mathbf{S}^H \mathbf{y}_m}{\left\|\mathbf{S}\right\|_F^2} \tag{4-52}$$

Substituting (4-52) into (4-49) yields

$$C_2(\omega_m) = \mathbf{y}_m^H \left[\mathbf{I} - \mathbf{S}\mathbf{e}(\omega_m) \frac{\mathbf{e}^H(\omega_m)\mathbf{S}^H}{\|\mathbf{S}\|_F^2} \right] \mathbf{y}_m \tag{4-53}$$

Note that this criterion is similar to that in (4-14). Minimizing (4-53) is equivalent to maximizing

$$C_3(\omega_m) = \mathbf{y}_m^H \mathbf{S}\mathbf{e}(\omega_m)\mathbf{e}^H(\omega_m)\mathbf{S}^H \mathbf{y}_m \tag{4-54}$$

Furthermore,

$$C_3(\omega_m) = \left\| \mathbf{e}^H(\omega_m)\mathbf{S}^H \mathbf{y}_m \right\|^2 \tag{4-55}$$

This can also be expressed as

$$C_3(\omega_m) = \left| \sum_{k=-N/2}^{N/2-1} S_k^* Y_{m,k} e^{-j\omega_m k} \right|^2 \tag{4-56}$$

Note that (4-56) can be evaluated for multiple ω_m candidates using the FFT (or the Goertzel algorithm, if the search interval is sufficiently limited).

The WRELAX algorithm evaluates (4-56) and (4-52) and updates $\hat{a}_m$ and $\hat{\omega}_m$ for $m \in 1{:}L$, based on $\mathbf{y}_m$ computed from (4-49) and current estimates, $\hat{\mathbf{a}}$ and $\hat{\boldsymbol{\omega}}$. The evaluation process is iterated until it reaches "practical convergence" or some threshold criterion.

4.3.3 Algorithm Performance on Known Signals

This section demonstrates the ability of the MODE-WRELAX algorithm by applying it to arbitrary – but known – overlapping pulses. First, consider a discrete raised-cosine reference pulse

$$s_n = \begin{cases} 0.5(1 - \cos 0.2\pi n), & 0 \le n < 10 \\ 0, & \text{elsewhere} \end{cases} \tag{4-57}$$

The pulse waveform and its 512-point DFT magnitude spectrum are shown in Figure 4-1(a) and Figure 4-1(b), respectively. To construct a composite of overlapping pulses, based on the given reference pulse, we arbitrarily selected $L = 3$, $\mathbf{a} = [1 \quad 1.2 \quad 0.2]$, and $\boldsymbol{\tau} = [5 \quad 7 \quad 20]$. Each pulse $y_{l,n}$

is plotted in different color in Figure 4-2(a), and the resulting linear combination y_n is shown in Figure 4-2.

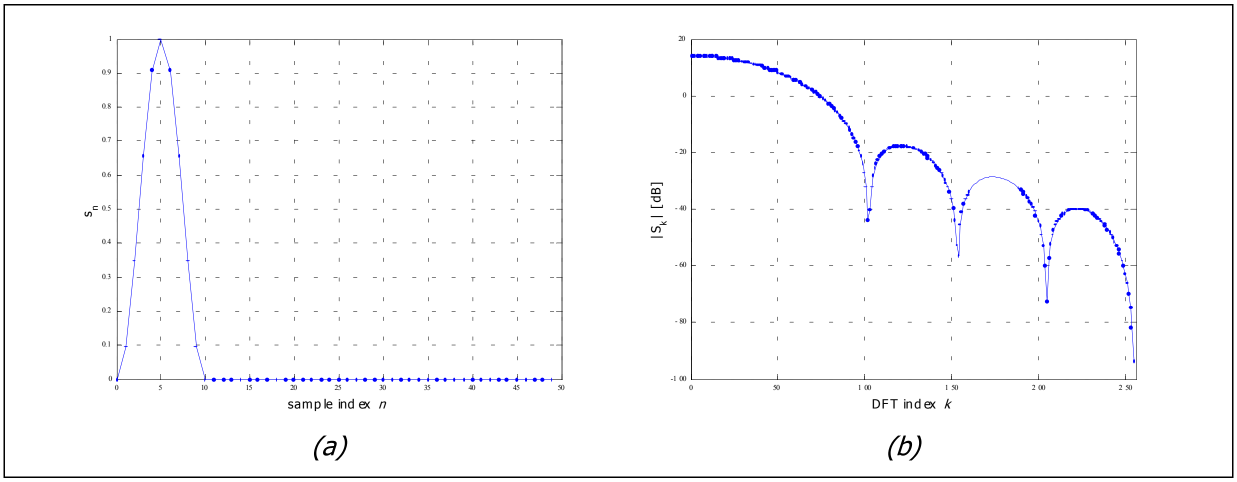

Figure 4-1: The reference pulse for MODE-WRELAX experiment 1 (a) and its 512-point DFT magnitude spectrum in dB (b) (only positive frequencies shown).

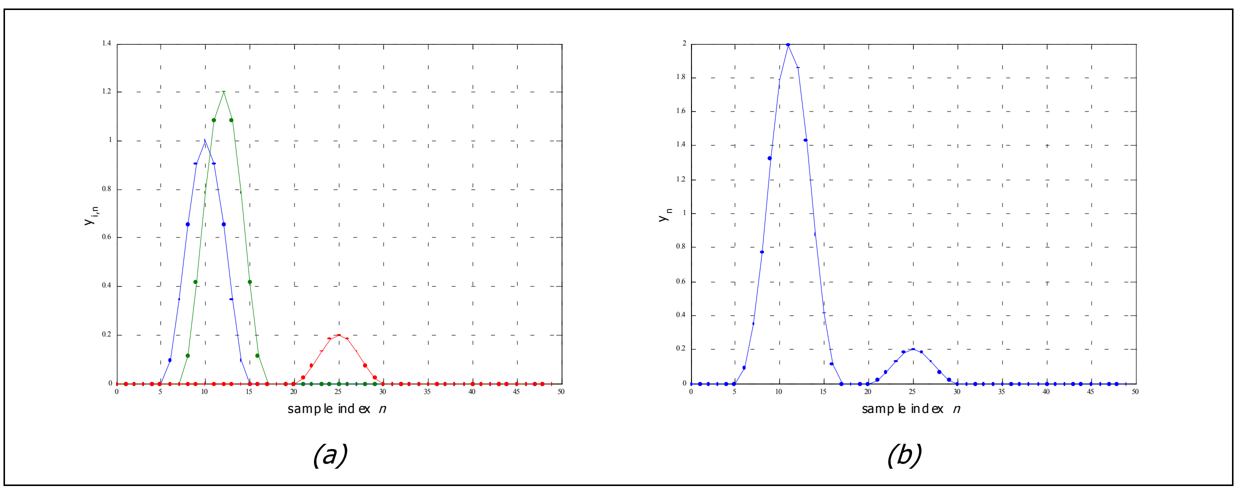

Figure 4-2: MODE-WRELAX Experiment 1 objective signal — individual pulses (a); and composite signal (b).

As shown in Figure 4-1(b), the reference pulse contains less energy at the higher frequencies than at the lower ones. Since the MODE algorithm is sensitive to low energy content in a signal (*i.e.* relative to its maximum energy) masking of the low-energy components – here, those at the higher frequencies – is desired. In this example, the $k = 0:40$ samples were utilized, while all other sample points were masked.

Under the assumption that we know the number of constituent pulses (*i.e.* $\hat{L} = 3$) and noise-free measurements, the MODE-WRELAX estimation result for each parameter is listed in Table 4-1. In the table the results from MODE itself, as well as from WRELAX with arbitrary initial conditions (±1%, ±5% and ±15% off the actual value) are presented.

Table 4-1: MODE-WRELAX experiment 1 — parameter estimation results ($\hat{L}$ = 3 & SNR = ∞).

Algorithm	$y_{1,n}$		$y_{2,n}$		$y_{3,n}$	
	τ	a	τ	a	τ	a
True Solution	5	1	7	1.2	20	0.2
MODE	5.000000	1.000000	7.000000	1.200000	20.000000	0.200000
WRELAX (with i.c. of ±1% of actual)	4.994812	0.995382	6.995706	1.204610	19.999966	0.200000
WRELAX (with i.c. of ±5% of actual)	4.909160	0.922571	6.929661	1.277297	19.999386	0.200007
WRELAX (with i.c. of ±25% of actual)	5.436810	1.462732	7.550871	0.735106	20.003009	0.199934
MODE-WRELAX	5.000000	1.000000	7.000000	1.200000	20.000000	0.200000

It is quite noticeable that the MODE algorithm works perfectly in the noiseless environment. Also, a degradation of the WRELAX algorithm solution is observed as the initial conditions are moved farther away from the true solution. With the initial condition off by 25% of the true solution, WRELAX no longer delivers the desired solution for the two pulses that are strongly overlapping. The latter is most likely due to the existence of multiple extrema of the criterion function. Lastly, the MODE-WRELAX solution does not require any effort by the WRELAX algorithm since the MODE algorithm solution leaves no room for improvement by WRELAX.

Furthermore, the performance of both the MODE and MODE-WRELAX algorithms is evaluated under slightly noisy conditions. Figure 4-3 shows the estimated parameters with the composite signal in Figure 4-2(b) contaminated by additive white Gaussian noise (AWGN) with standard deviation σ of 10^{-5}. While the third small isolated pulse is consistently estimated correctly, the parameter estimates for the first two pulses indicate large fluctuation mainly due to their closeness to each other.

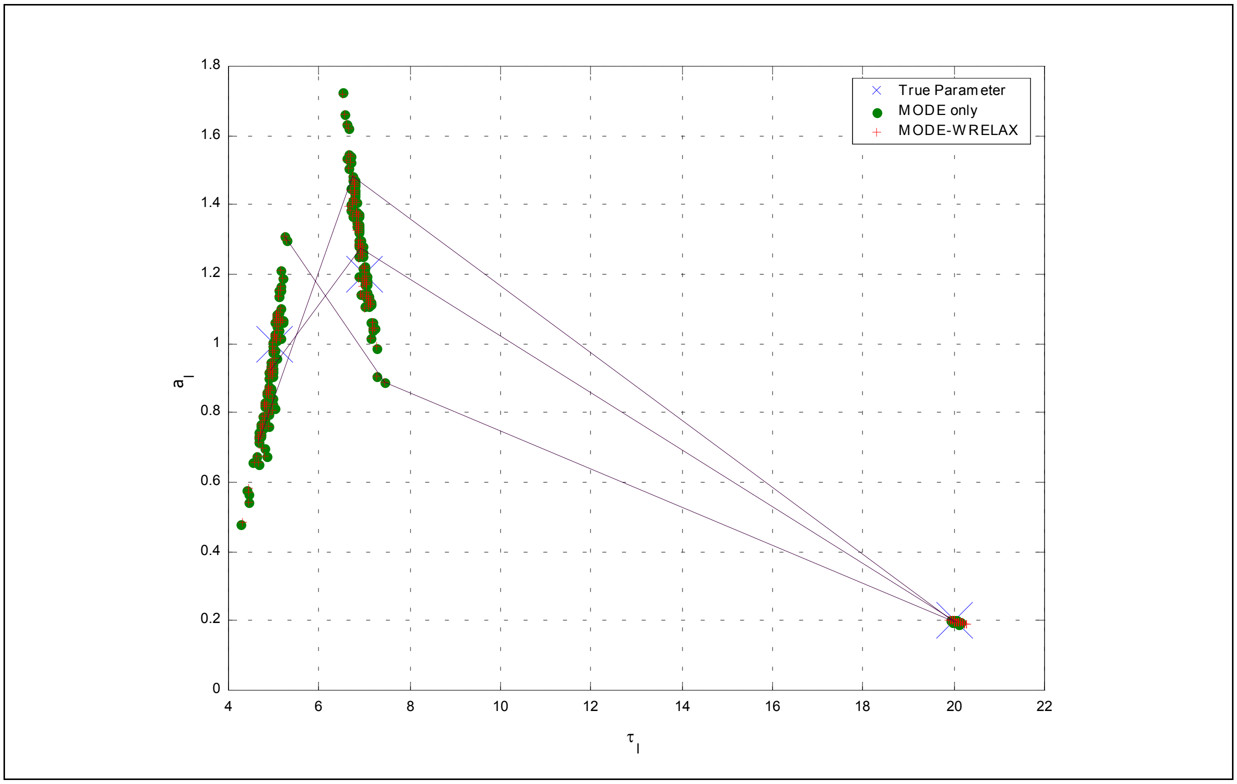

Figure 4-3: Experiment 1 — Monte-Carlo (x100) MODE-WRELAX estimation results (AWGN with σ = 10^{-5}). Line indicates compensatory behavior of estimates.

Another important issue is the behavior of the estimate when the number of pulses is not known. Table 4-2 shows the MODE and MODE-WRELAX estimates for different estimated number of pulses, namely $\hat{L}$= 2, 4, and 6. If the number of pulses is underestimated, the correct parameters cannot be obtained at all, and some sort of averaged representation results. However, in case of overestimation, all the pulses are successfully identified, together with some additional (spurious) signals that have essentially zero amplitude.

Table 4-2: MODE-WRELAX experiment 1
Parameter estimation results 2 ($\hat{L}$ = 2, 4, and 6 & SNR = ∞). (bold face – correct estimations)

$\hat{L}$	**Algorithm**	τ	**a**
	True Solution	[5 7 20]	[1 1.2 0.2]
2	MODE	[5.6406 10.5074]	[1.9888 0.2596]
	MODE-WRELAX	[5.4609 7.5842]	[1.4878 0.7082]
4	MODE	[-55.687 **5.000 7.000 20.000**]	[5.275×10^{-17} **1.000 1.200 0.2**]
	MODE-WRELAX	[-57.749 **5.000 7.000 20.000**]	[-2.514×10^{-16} **1.000 1.200 0.2**]
6	MODE	[-52.05 -28.49 **5.00 7.00 20.00** 58.90]	[-2.11×10^{-16} -2.12×10^{-16} **1.00 1.20 0.20** 1.23×10^{-16}]
	MODE-WRELAX	[-52.64 -27.55 **5.00 7.00 20.00** 57.83]	[$-3.04\times10^{-16}$$-4.48\times10^{-16}$ **1.00 1.20 0.20** 5.04×10^{-16}]
	MODE-WRELAX	[-57.16 -56.26 -37.83 **5.00 7.00 20.00**]	[1.24×10^{-12} -1.24×10^{-12} 4.26×10^{-14} **1.00 1.20 0.20**]

The pulses in the previous example have a finite duration, which does not represent the typical TDR response of a TP loop well. Instead, each overlapping pulse contains an exponential decay. To illustrate the MODE-WRELAX algorithm's capability on an exponentially decaying function, we present another experiment with a reference signal that resembles a charge-discharge type pulse:

$$s_n = \begin{cases} 0, & n < 0 \\ 1 - e^{-0.9n}, & 0 \le n < 10 \\ \left[1 - e^{-9}\right] e^{-0.5(n-10)}, & n \ge 10 \end{cases} \tag{4-58}$$

as shown in Figure 4-4(a). Again, the magnitude spectrum is provided in Figure 4-4(b). To construct overlapping pulses based on the reference pulse, we again selected L = 3, $\mathbf{a} = \begin{bmatrix}1 & 1.2 & .2\end{bmatrix}$, and $\boldsymbol{\tau} = \begin{bmatrix}5 & 7 & 20\end{bmatrix}$. The individual pulses and the resulting linear combination $y(t)$ are shown in Figure 4-5(a) and Figure 4-5 (b), respectively.

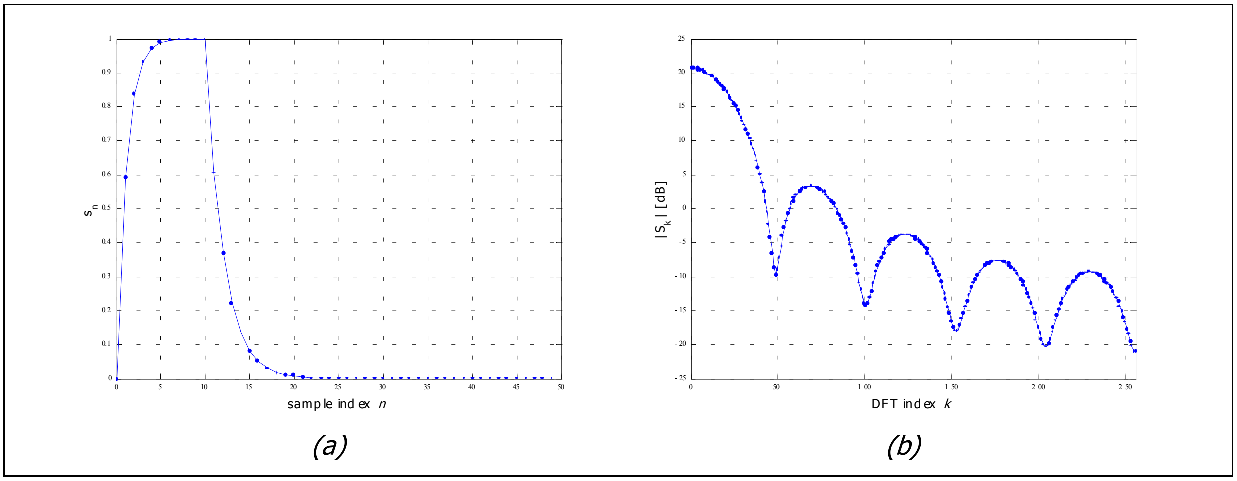

Figure 4-4: The reference pulse for MODE-WRELAX experiment 2 (a) and its 512-point DFT magnitude spectrum in dB (b) (only positive frequencies shown).

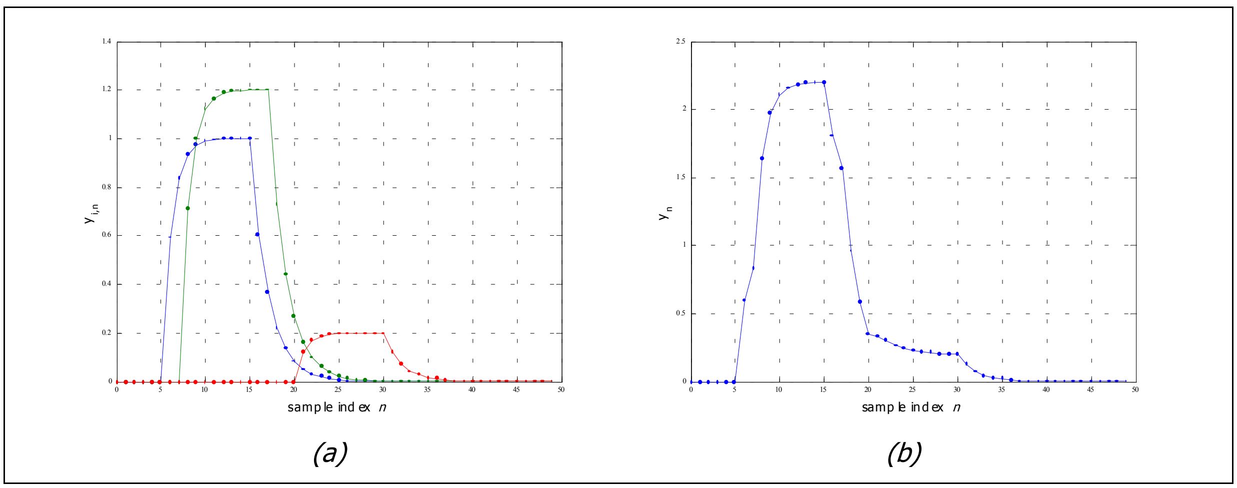

Figure 4-5: MODE-WRELAX experiment 2 objective signal — individual pulses (a); and composite signal (b).

The same masking scheme that was used for the measured signal in the first experiment was applied in this example since both reference magnitude spectra are similar. Table 4-3, Figure 4-6, and Table 4-4 show the parameter estimation results that correspond to those of the first experiment in Table 4-1, Figure 4-3, and Table 4-2, respectively. Note that the estimation accuracy is very high with the correct – or higher – number of pulses assumed for the MODE and MODE-WRELAX algorithms.

Table 4-3: MODE-WRELAX experiment 2 — parameter estimation results 1 ($\hat{L} = 3$ & SNR = ∞).

Algorithm	$y_{1,n}$		$y_{2,n}$		$y_{3,n}$	
	τ	a	τ	a	τ	A
True Solution	5	1	7	1.2	20	0.2
MODE	5.000000	1.000000	7.000000	1.200000	20.000000	0.200000
WRELAX (with i.c. of ±1% of actual)	5.005086	1.004736	7.004440	1.195285	20.001693	0.199965
WRELAX (with i.c. of ±5% of actual)	4.976393	0.978272	6.979788	1.221629	19.992125	0.200162
WRELAX (with i.c. of ±25% of actual)	4.553201	0.659329	6.703037	1.538006	19.851768	0.202790
MODE-WRELAX	5.000000	1.000000	7.000000	1.200000	20.000000	0.200000

Table 4-4: MODE-WRELAX experiment 2
parameter estimation results 2 ($\hat{L}$ = 2, 4, and 6 & SNR = 0 dB). (bold face – correct estimations)

$\hat{L}$	**Algorithm**	τ	**a**
	True Solution	[5 7 20]	[1 1.2 0.2]
2	MODE	[5.82 14.73]	[2.09 0.22]
	MODE-WRELAX	[6.07 18.98]	[2.15 0.21]
4	MODE	[-46.52 **5.00 7.00 20.00**]	[-7.66×10^{-14} **1.00 1.20 0.20**]
	MODE-WRELAX	[-47.67 **5.00 7.00 20.00**]	[-5.37×10^{-14} **1.00 1.20 0.20**]
6	MODE	[-59.10 -56.08 -37.42 **5.00 7.00 20.00**]	[1.09×10^{-13} -1.23×10^{-13} 3.75×10^{-14} **1.00 1.20 0.20**]

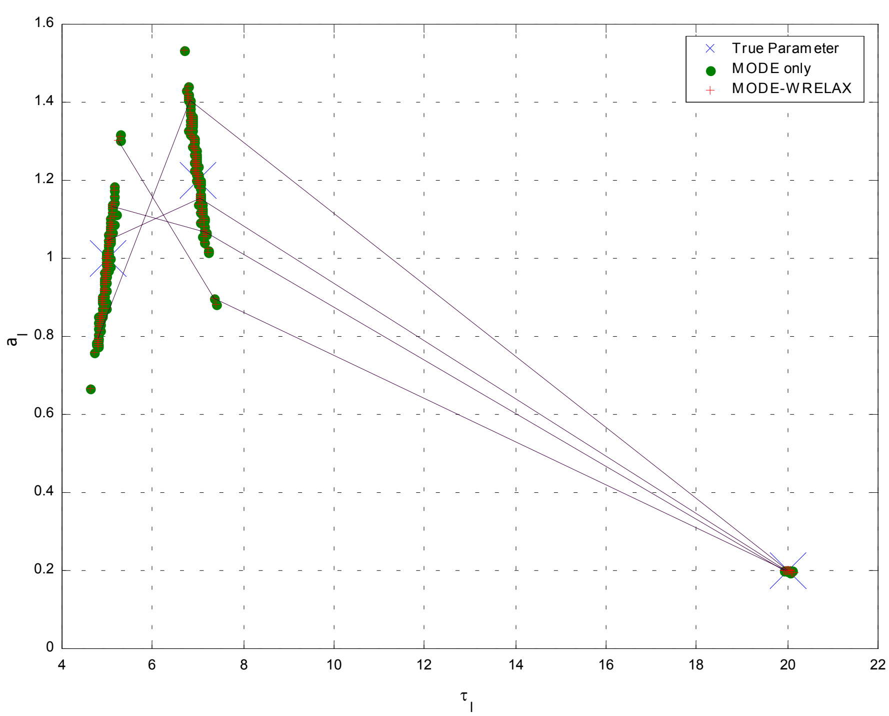

Figure 4-6: Experiment 2 — Monte-Carlo (x100) MODE-WRELAX estimation results (AWGN w/σ = 10^{-5}). Line indicates compensatory behavior of estimates.

4.4 TDR Reflection Decomposition Using MODE-WRELAX

If the TDR reflection pulses satisfy the underlying assumption that the closely spaced pulses differ only in their delay and amplitude and have the same shape, the MODE-WRELAX algorithm is expected to work properly. In this section, the MODE-WRELAX algorithm is applied to a couple of TDR responses for some loop configurations that are considered for loop identification, with the idea of getting a preliminary evaluation of its usefulness in the identification process.

4.4.1 Methodology

To apply the MODE-WRELAX algorithm to the TDR-based loop identification process, the application procedure must be established first. Specifically, assignments of the reference signal s_n and objective signal y_n for the MODE-WRELAX are essential. Under the iterative identification procedure presented in Chapter 3, MODE-WRELAX is the ideal candidate for the reflection detection procedure. Instead of locating one reflection at a time, the MODE-WRELAX algorithm is capable of detecting multiple, overlapping reflections in a single algorithm execution.

One set of prospects for s_n and y_n is the full TDR response and the TDR input (raised cosine) pulse. However, in Chapter 2, we have already shown that separable TDR reflections undeniably have a different shape, which fundamentally violates the MODE-WRELAX assumption. Also, all reflections possess the dispersive tail, which the input signal (raised-cosine pulse) does not have. These observations suggest that the reference signal cannot be the TDR input signal so that processing the entire TDR response altogether is unsuitable.

The better alternative is to decompose the residual signal in (3-1), between the measurement and the latest partial model, with an artificial reference pulse created on the basis of the initial length estimation procedure described in Section 3.4.1. In other words, the MODE-WRELAX algorithm is used for refinement of the initially detected reflection and to additionally detect possible later reflections.

Another issue is the selection of *L*, the number of overlapping pulses. Theoretically there is an infinite number of TDR reflections, but most are very small compared to the dominant ones. For the evaluation of the suitability of the MODE-WRELAX algorithm, the reflection count will be estimated via visual inspection.

4.4.2 Decomposition Experiment

The evaluation of the algorithm in TDR reflection decomposition is carried out with the loop shown in Figure 4-7(a), which is similar to the CSA #1 loop, but with much shorter segments. Suppose the first iteration of the identification cycle has successfully identified the 26-AWG infinitely long segment attached to the measurement node. The TDR response is simulated at 40 MHz for 2^{15} samples. The TDR responses of the complete loop and model, both from Node 1, are plotted in Figure 4-8.

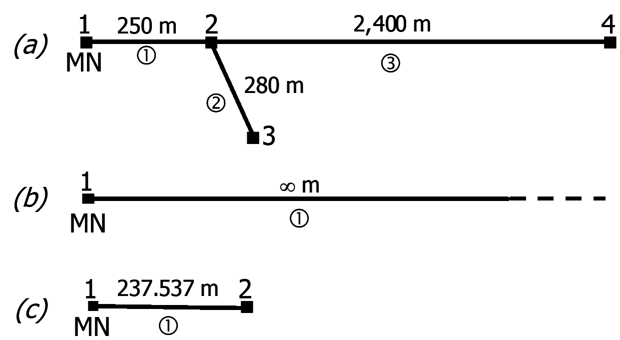

Figure 4-7: MODE-WRELAX test loop for near-end reflection decomposition (a), partial model after 1st iteration (b), and model with which reference signal is simulated (c). (All line types: ANSI PIC 26 AWG)

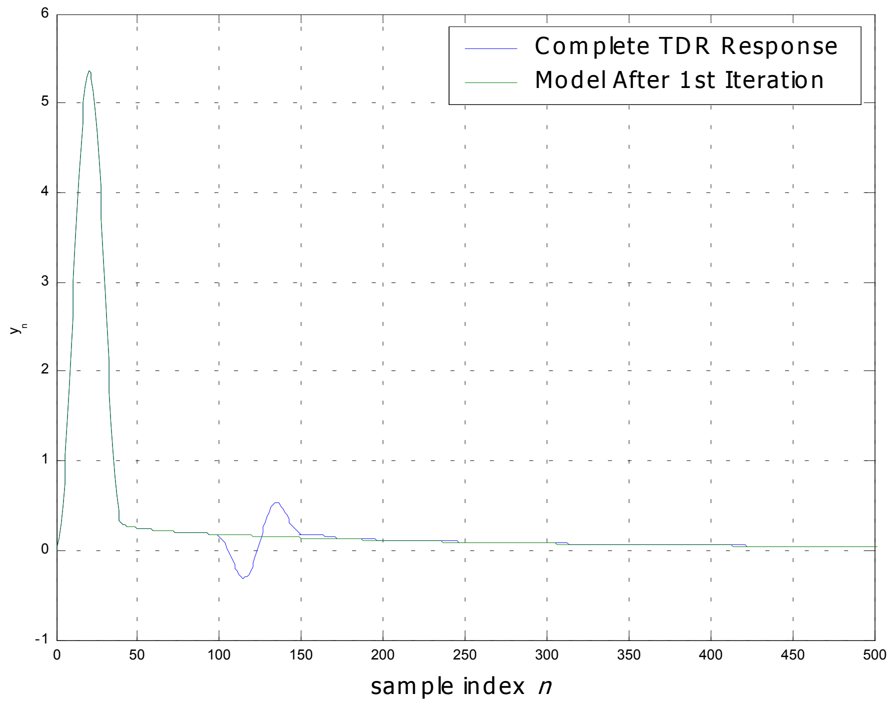

Figure 4-8: Complete TDR responses of the loop in Figure 4-7(a) and of the partial model in Figure 4-7(b).

Furthermore, the reflection detection procedure returns $n_r = 101$ corresponding to the initial length estimate of 237.537 m. With that length estimate, the reference loop in Figure 4-7(c) is constructed based on the model, and the initial reflection from Node 2 of the reference loop is used as the reference signal. Both the reference and residual (overlapping) signal are plotted in Figure 4-9. Moreover, Figure 4-10 illustrates the underlying dominant reflections that are overlapping. The two overlapping reflections correspond to Node 2 and Node 3. With an additional reflection visible starting at n = 150, there are three visible reflections that need to be estimated.

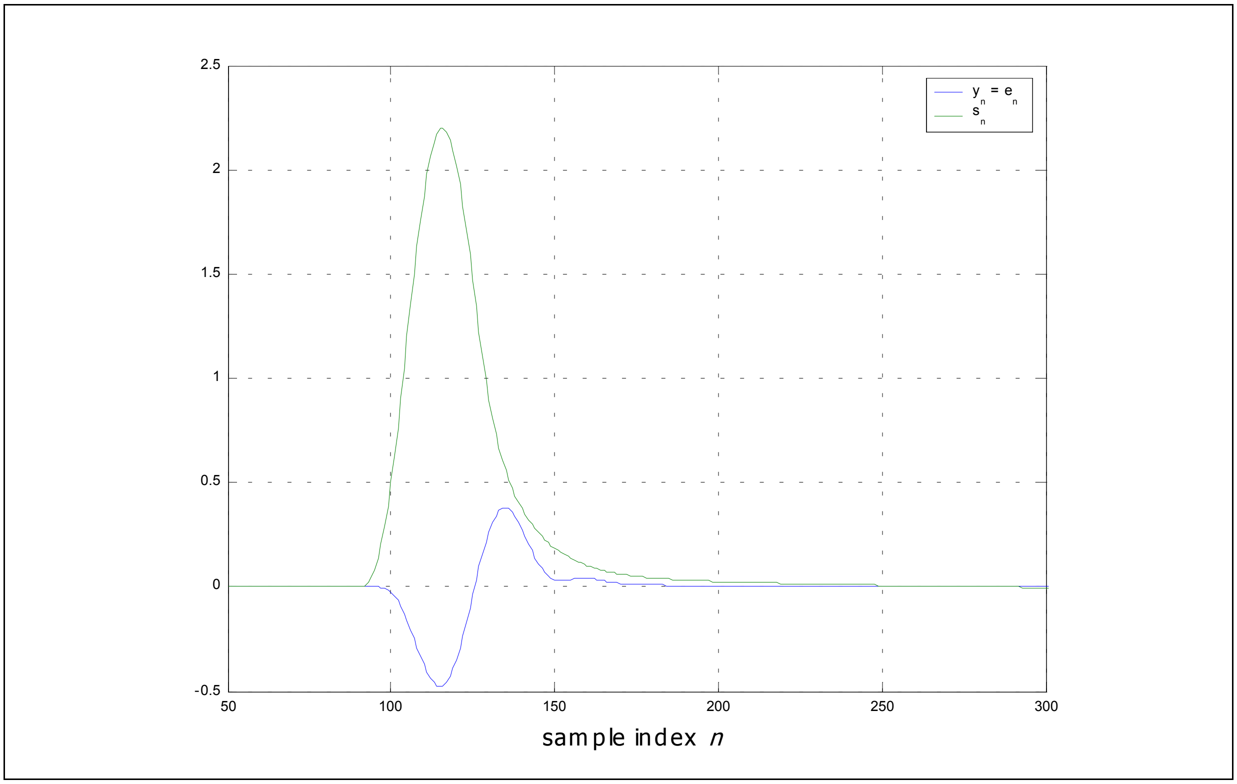

Figure 4-9: Residual (blue) and reference pulse (green).

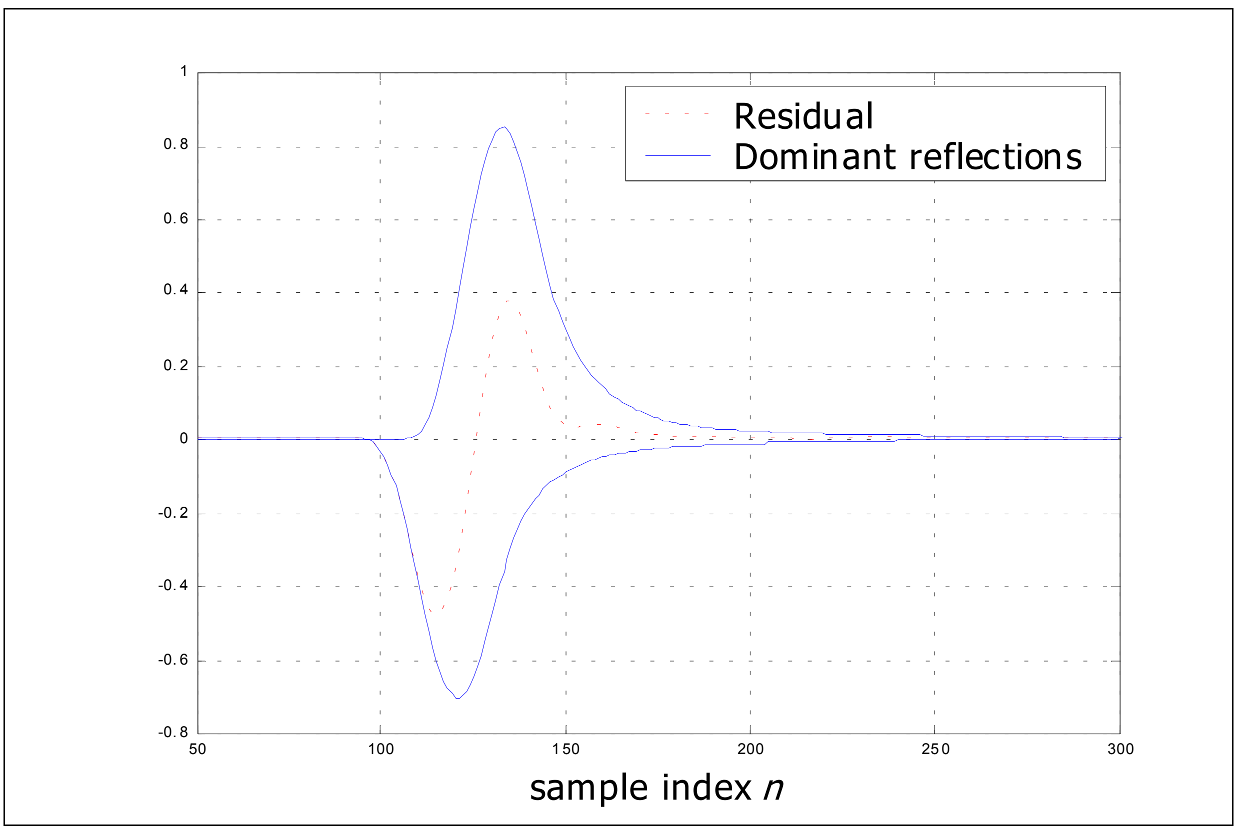

Figure 4-10: Dominant reflections hidden in the residual signal.

The signals in Figure 4-9 and estimated number of dominant reflections, $\hat{L} = 3$, provide all the input quantities for the MODE-WRELAX algorithm. The first step is to determine the frequency sample points to use for the MODE-WRELAX algorithm. Based on the magnitude spectra of the signals, as shown in Figure 4-11, 101 samples from the 2^{15}-point DFT over k = 100 to k = 500, taking only samples that are divisible by 4 (this effectively reduces the number of frequency points to N = 2^{13}).

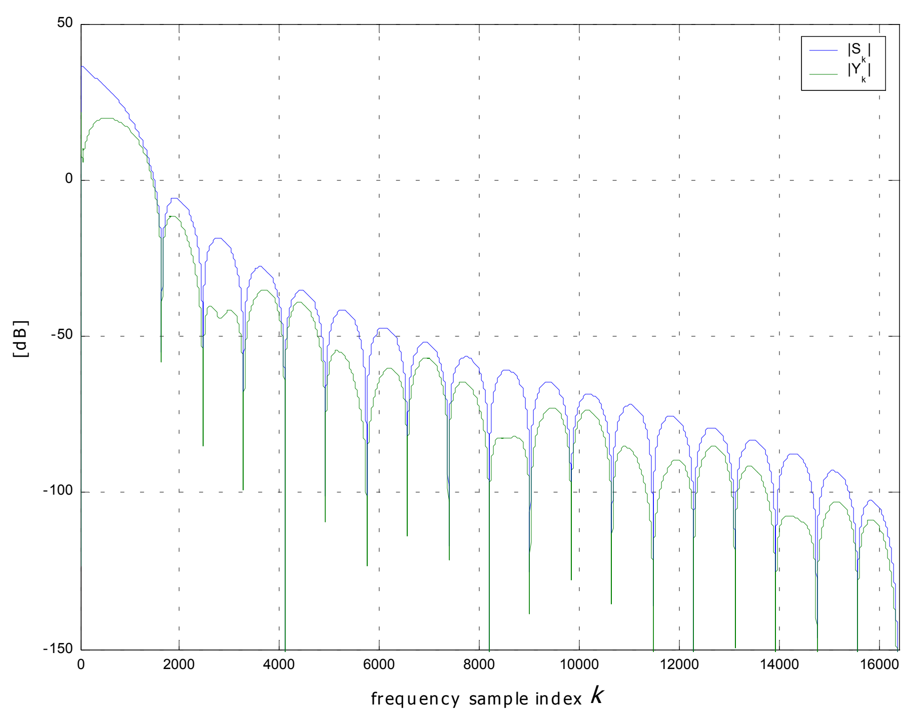

Figure 4-11: Magnitude spectra of reference signal (blue) and overlapping signal (green).

With these spectrum samples, both the MODE algorithm itself and the MODE-WRELAX algorithm are applied six times, for a different assumed number of reflections $\hat{L}$= 2:7. The estimation results are tabulated in Table 4-9, and their corresponding reconstructed composite signals are shown in Figure 4-12. The results are not encouraging. The reconstructed superimposed signals are considerably different from the original in all cases. The first thing to notice is that the a_i's are complex, and the individual reconstructed reflections appear to be substantially different from either the reference reflection or the overlapping reflections. Furthermore, the delay estimates do not correspond to the expected values. From Figures 4-9 and 4-10, the offsets between the reference reflection and the three visible reflections are about 5, 20, and 60 samples (there is another hidden reflection around 40). Only the Node 2 reflection (the negative reflection) seems to be identified (τ_i = ~6.5) when the MODE algorithm itself is used. Despite the obvious failure of the TDR reflection decomposition attempt, there are two phenomena worth noting. First, the MODE estimates for $\hat{L} \geq 4$ are consistent; *i.e.*, approximately the same estimates are found for all estimated number of reflections. Secondly, the WRELAX algorithm flattens the signal tails that are introduced by the complex amplitude parameter even though the overall signals are worse than the MODE estimates.

Table 4-5: MODE-WRELAX estimates for TDR decomposition.

$\hat{L}$	$y_{i,n}$	MODE only			MODE-WRELAX		
		τ_i	Re{a_i}	Im{a_i}	τ_i	Re{a_i}	Im{a_i}
2	$y_{1,n}$	1.784	-0.032686	-0.14917	8.0807	0.12554	-0.037364
	$y_{2,n}$	41.798	0.018165	-0.011187	78.864	-0.0085676	-0.00060532
3	$y_{1,n}$	2.612	-0.0051698	-0.15379	8.0867	0.12557	-0.037174
	$y_{2,n}$	36.228	0.0076525	-0.019498	78.883	-0.0085896	-0.00063546
	$y_{3,n}$	551.57	0.0011731	0.00063505	583.63	-0.00053411	-0.00037161
4	$y_{1,n}$	6.8466	0.17762	-0.31629	14.378	-0.063342	-0.063009
	$y_{2,n}$	10.433	-0.21499	0.14868	18.681	-0.032294	0.1108
	$y_{3,n}$	101.9	-0.0014965	-0.0044398	82.539	0.00045566	-0.0036192
	$y_{4,n}$	978.91	0.00010435	0.00026378	995.76	-0.00023087	-0.0004397
5	$y_{1,n}$	6.6404	0.15401	-0.29975	9.3825	0.010585	-0.0030831
	$y_{2,n}$	10.558	-0.1939	0.13378	9.7742	0.10681	0.016817
	$y_{3,n}$	101.84	-0.0015384	-0.0044173	93.221	0.010223	-0.002072
	$y_{4,n}$	979.16	0.00012363	0.00023412	992.48	-0.00074476	-0.00016423
	$y_{5,n}$	-3885.7	0.00080272	-0.00040774	-3864.9	-0.0067	-0.0015883
6	$y_{1,n}$	6.5973	0.14934	-0.29556	12.599	0.066824	0.052543
	$y_{2,n}$	10.599	-0.18945	0.12986	18.201	-0.016896	0.0084107
	$y_{3,n}$	101.85	-0.0015319	-0.0043592	88.243	0.0080102	-0.012509
	$y_{4,n}$	979.04	0.00013206	0.00023284	999.45	-0.00012991	-0.0016724
	$y_{5,n}$	-1819.8	-0.00048815	0.001168	-1833.8	-0.0057597	0.0021237
	$y_{6,n}$	-3495.1	-0.00094712	-0.00018915	-3457.9	-0.0024095	8.8839×10^{-5}
7	$y_{1,n}$	6.5362	0.14271	-0.28621	18.265	0.027235	-0.083729
	$y_{2,n}$	10.725	-0.18241	0.11993	22.454	-0.083902	0.028495
	$y_{3,n}$	101.89	-0.0015388	-0.004399	89.738	0.0095783	-0.0040779
	$y_{4,n}$	975.35	0.00029614	0.0005286	1003	0.00094242	-0.00095456
	$y_{5,n}$	-1719.9	-0.00062568	0.00039941	-1678.8	0.00065938	0.00098044
	$y_{6,n}$	-3378.4	0.00029262	-0.00014612	-3382.1	-9.6238×10^{-5}	0.00070239
	$y_{7,n}$	3510.5	0.00074755	2.0378×10^{-5}	3510.9	0.00024211	0.00047585

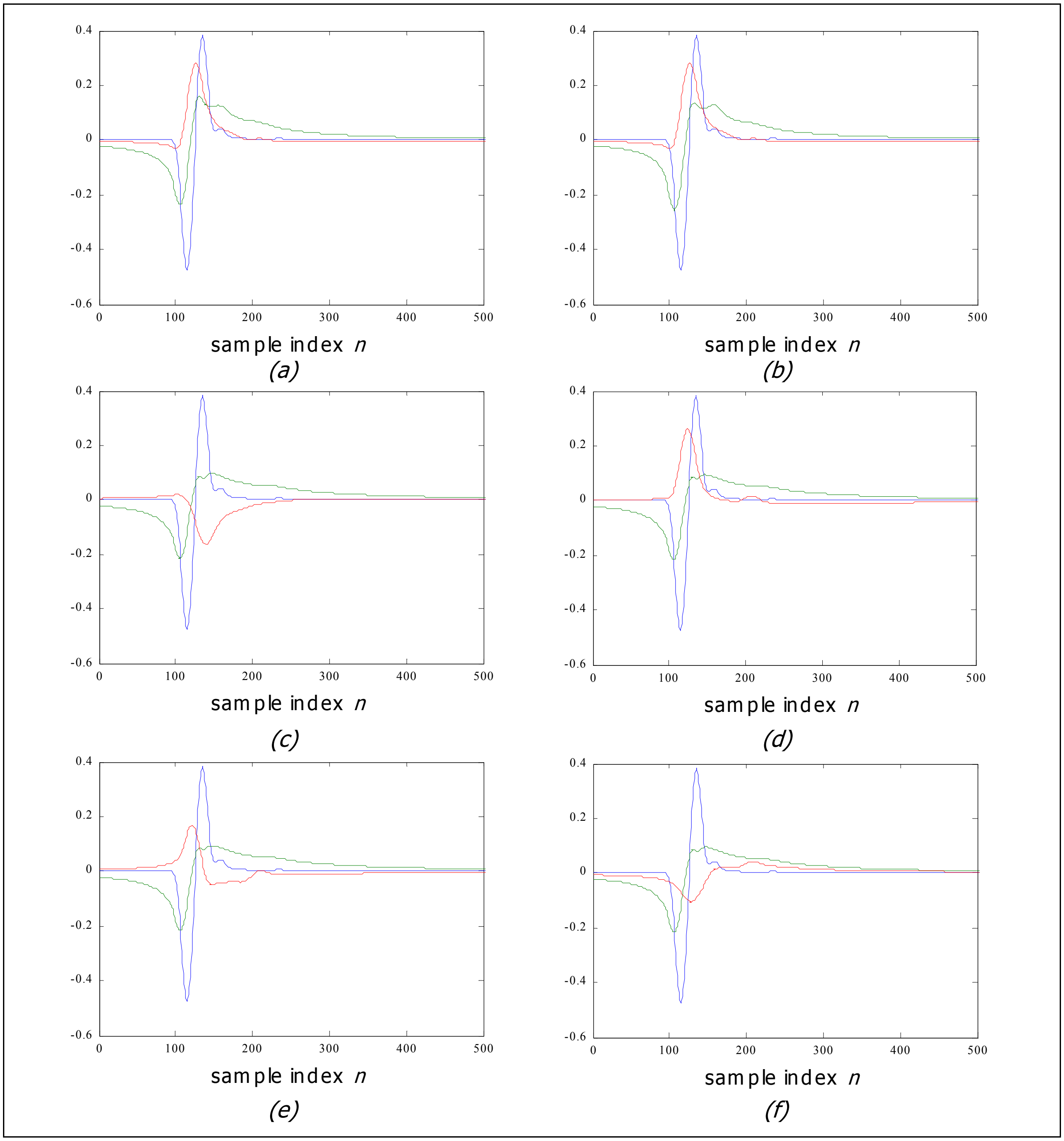

Figure 4-12: The MODE-WRELAX estimation results — actual residual (blue), MODE reconstructed residual (green), and MODE-WRELAX reconstructed residual (red) — $\hat{L} = 2$ *(a),* $\hat{L} = 3$ *(b),* $\hat{L} = 4$ *(c),* $\hat{L} = 5$ *(d),* $\hat{L} = 6$ *(e), and* $\hat{L} = 7$ *(f).*

Two possible reasons for the above poor results are:

- Assumption violation — reflection shapes vary significantly;
- Inappropriate selection of frequency samples.

With the selection of the frequency range where most energy is concentrated, for both the reference and the composite signal, the second possibility is unlikely. On the other hand, our observation of the shape difference between the original and reconstructed signals indicates that the signal model in (4-1) does not hold for the TDR reflections. To further verify this hypothesis, the Fourier domain model in (4-3) is examined. Dividing both sides of (4-3) by S_k and assuming complex a_i yields

$$\frac{Y_{i,k}}{S_k} = |a_i| e^{j(\angle a_i - \omega_i k)} \tag{4-59}$$

In other words the magnitude of the ratio is constant while the phase of the ratio is affine. Figure 4-13 shows the above ratio between the analytically extracted TDR reflections in Figure 4-10 and the reference reflection in Figure 4-9. While the phase behavior in Figure 4-9(b) obeys the assumption, the magnitude ratio is far from being constant. Comparison between $Y_{r1,k}/S_k$ and $Y_{r2,k}/S_k$ indicates that the further a reflection is from the reference reflection, the more deviation from the model occurs.

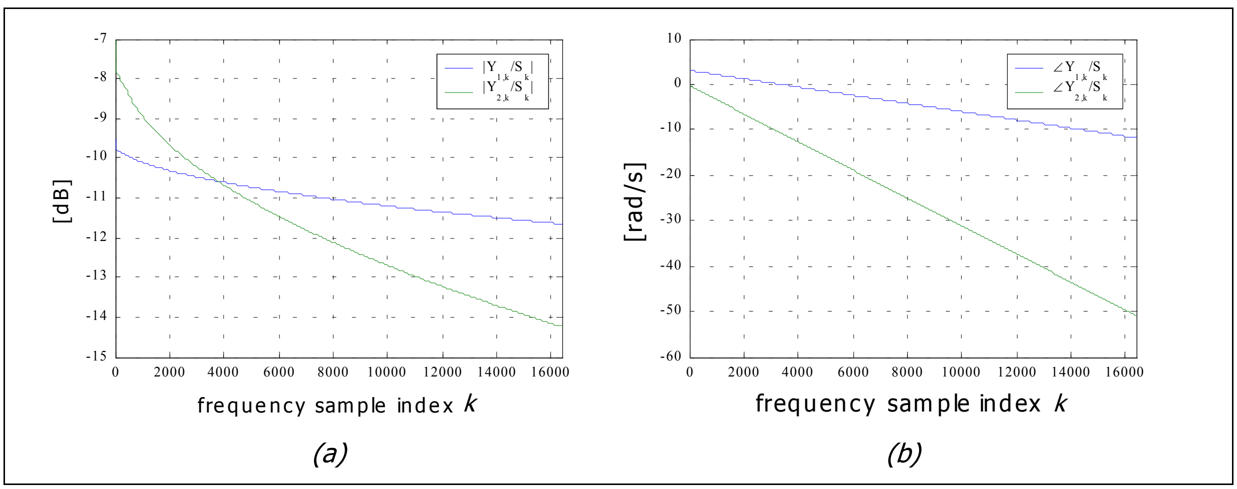

Figure 4-13: The spectral ratio of individual overlapping reflections to the reference.

The above observation suggests that the (4-3) model does not portray the TDR reflection behavior, and thus the MODE-WRELAX algorithm cannot be applied directly. However, if the time-varying or dispersive nature of the TDR reflections can be included in the model, the subspace-method based approach to separate TDR reflections could be effective.

4.5 Problem Reformulation — TP Analysis for Dispersion Modeling

In the last section, the MODE-WRELAX algorithm, which is designed to decompose a superposition of delayed and scaled versions of a known reference signal, was found not effective in decomposing TDR reflections. The dispersive nature of the TDR reflections prevents the MODE-WRELAX algorithm assumption (*i.e.* all pulse shapes are identical) from being satisfied in general. To address this shortcoming of the MODE-WRELAX algorithm and to adopt the reflection ratio observed in Figure 4-13, the MODE-type algorithm is introduced toward solving the TDR reflection decomposition problem. The MODE-type algorithm, which was originally developed for damped, undamped, and explosive sinusoids, is capable of modeling the particular kind of dispersion where the dispersed signal's magnitude spectrum rolls off in exponentially decaying fashion. The model for the MODE-type algorithm is defined as follows, in the Fourier domain,

$$Y_k = S_k \sum_{l=1}^{L} a_l \rho_l^k + E_k \tag{4-60}$$

where

$$\rho_l = \left[\zeta_l \exp\left(-j\tau_l\right)\right]^{\frac{2\pi f_s}{N}} \tag{4-61}$$

with damping (dispersion) factors $\{\zeta_l\}_{l=1}^{L}$. Note that $\angle\rho_l = \omega_l$.

Visual inspection of the ratio of the reflection spectra in Figure 4-13 immediately points out that (4-60) is not applicable over the entire frequency range of the spectrum, due to deviations for the low frequency range. Note that the magnitude part of (4-60) is affine in dB. However, if only the high frequency components are considered, the (4-60) model seems to agree with the TDR reflection characteristics. This assumption is verified in the next subsection with respect to the system block diagram derived from the bounce diagram in Section 2.6.

4.5.1 Analysis of Reflection Signal Models

To confirm the compatibility of the MODE-type model in (4-60) with TP loop reflections, individual building blocks of the TP loop block diagram — discussed in Section 2.6 — are evaluated. Recall that all TP loops can be modeled as a combination of subsystems as in Figure 2-18. Furthermore, a path on the system block diagram corresponds to a TDR reflection, and thus the reflection spectra are defined as the input spectrum multiplied by a cascade of TP loop blocks on its path. Therefore, if each possible TDR loop block can be modeled by (4-60), the ratio of any TDR reflections is also in compliance with (4-60).

System blocks to consider are those included in Figure 2-18, except for the source discontinuity transmission *A(f)* in Figure 2-18 (a). *A(f)* does not need to be considered since it is mutually included in all reflection spectra expressions, and hence the ratio of two reflections no longer includes the term. The others that need to be analyzed are

- Propagation block $e^{-2l\gamma}$ in Figure 2-18 (a);
  - Reflection function $\Gamma_{c1}(f)$ (2-16) at GC node in Figure 2-18 (d);
  - Transmission function $\mathrm{T}_{c1}(f) = 1 + \Gamma_{c1}(f)$ at GC node in Figure 2-18 (d);
  - Reflection function $\Gamma_{d1}(f)$ (2-17) at BT node in Figure 2-18 (e);
  - Transmission function $\mathrm{T}_{d1}(f) = 1 + \Gamma_{d1}(f)$ at BT node in Figure 2-18 (e).

For each case, combinations of two TP line types are considered (24 and 26 AWGs, with the much less used 22 AWG excluded for simplicity). The BT TP type combinations are listed in Table 4-6. The (4-60) model is fit to these TP frequency-domain characteristics over the arbitrarily selected frequency range, from 1 MHz to 2 MHz. Fitting (4-60) to the propagation block yields

$$e^{-2l\gamma(f)} \equiv a_p \rho_p^f \tag{4-62}$$

This is equivalent to the affine approximation of both attenuation and phase functions:

$$\alpha(f) \approx m_\alpha f + c_\alpha \tag{4-63}$$

and

$$\beta(f) \approx m_\beta f + c_\beta \tag{4-64}$$

where

$$m_\alpha f + c_\alpha \propto f \ln\left|\rho_p\right| + \ln\left|a_p\right| \tag{4-65}$$

and

$$m_\beta f + c_\beta \propto \angle\rho_p f + \angle a_p \,. \tag{4-66}$$

For the other blocks, magnitude and phase are separately fitted according to (4-60). The modeling results (in least squares sense) for all five cases are shown in Figures 4-14 – 4-26.

Table 4-6: Possible BT TP type combinations with 24 AWG and 26 AWG TP types. TP 1 leads the node and TPs 2 & 3 follow the node with respect to the measurement node.

Config.	TP 1	TP 2	TP 3
1	24 AWG	24 AWG	24 AWG
2	24 AWG	24 AWG	26 AWG
3	24 AWG	26 AWG	26 AWG
4	26 AWG	24 AWG	24 AWG
5	26 AWG	24 AWG	26 AWG
6	26 AWG	26 AWG	26 AWG

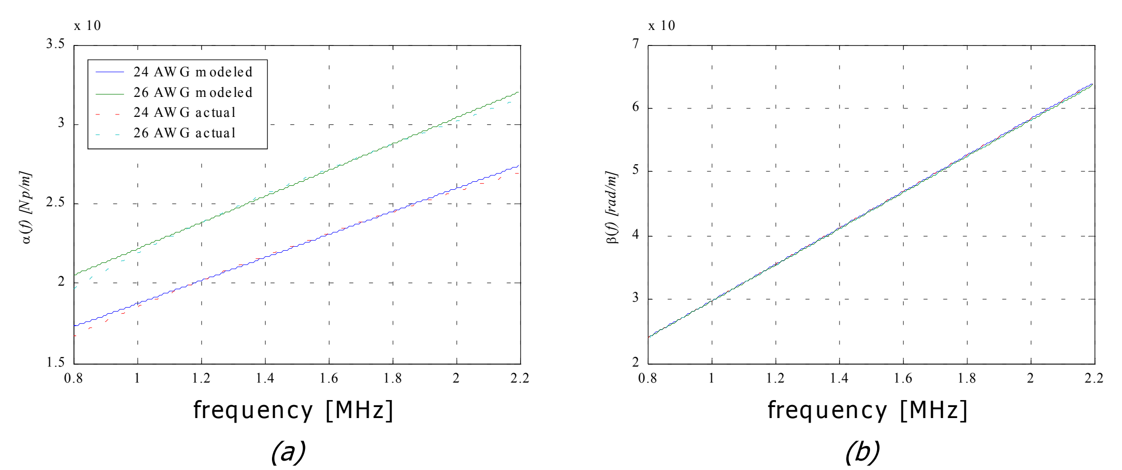

Figure 4-14: Least-square estimates of attenuation function (a) and phase function (b) 24 & 26 AWG TPs — modeled over 1 MHz to 2 MHz.

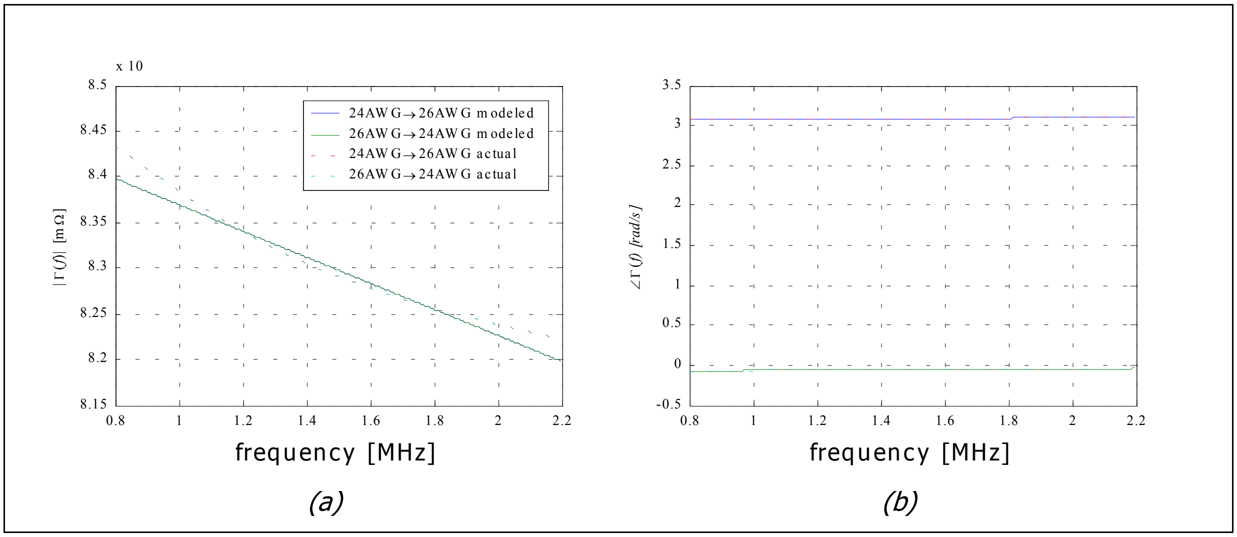

Figure 4-15: Least-squares estimates of magnitude (a) and phase (b) of the reflection function at GC node. Gauge change between 24 & 26 AWG TPs — modeled over 1 MHz to 2 MHz.

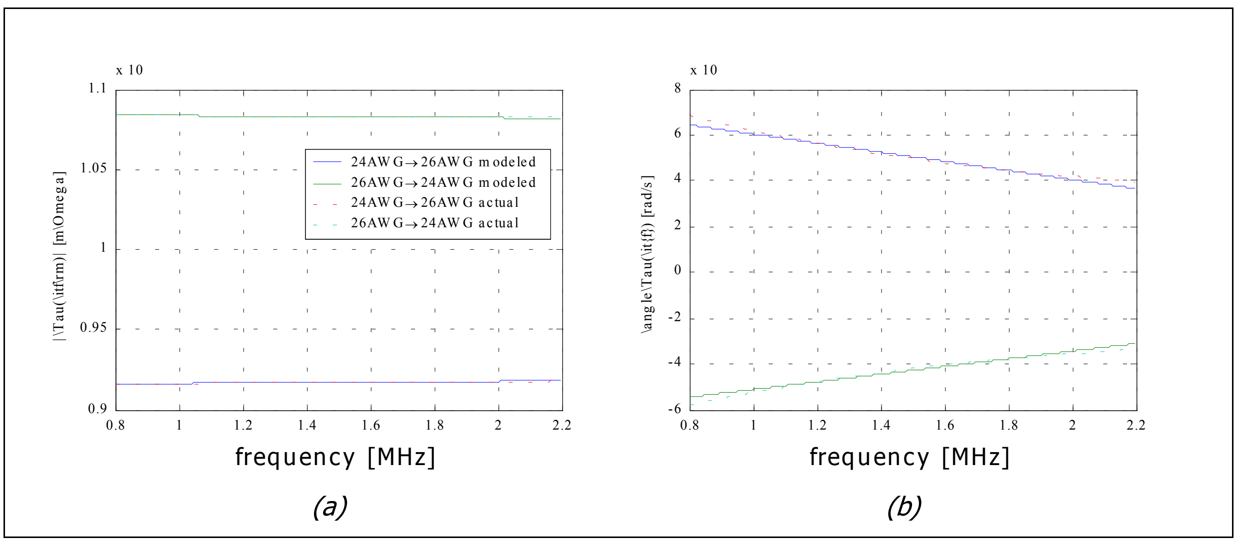

Figure 4-16: Least-squares estimates of magnitude (a) and phase (b) of the transmission function at GC node. Gauge change between 24 & 26 AWG TPs — modeled over 1 MHz to 2 MHz.

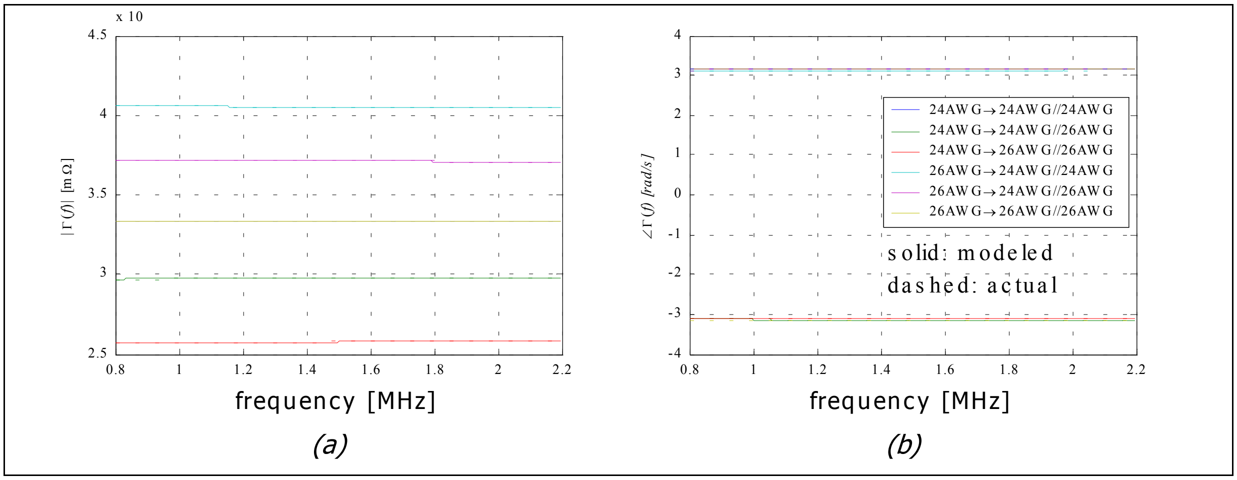

Figure 4-17: Least-squares estimates of magnitude (a) and phase (b) of the reflection function at BT node. Combination configuration defined in Table 4-6 — modeled over 1 MHz to 2 MHz.

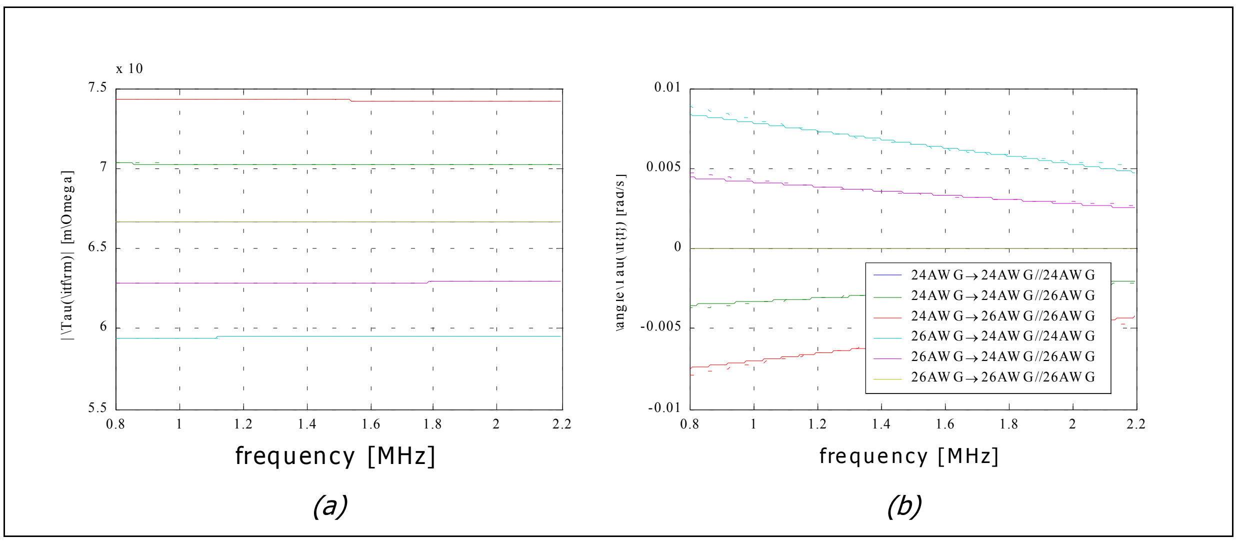

Figure 4-18: Least-squares estimates of magnitude (a) and phase (b) of the transmission function at BT node. Combination configuration defined in Table 4-6 — modeled over 1 MHz to 2 MHz.

All the fitting results demonstrate a good fit between the TP loop characteristics and the new signal model. Even though the frequency responses outside of the fitting region are noticeably different between the two, a good enough fit over the frequency region of 1 MHz to 2 MHz is obtained to proceed with the MODE-type algorithm implementation.

4.6 MODE-Type Algorithm

In the previous section, we have shown that the dispersive signal model (4-60) is indeed a good (though not perfect) model to apply for TDR reflection decomposition. This section introduces the MODE-type algorithm that can obtain the necessary parameters in the model. The MODE-type algorithm is a MODE based algorithm for decomposing linear combinations of damped, undamped or explosive modes [26]. The MODE-type algorithm shares the same roots [21] as the MODE algorithm used in the MODE-WRELAX algorithm. However, the MODE-type algorithm pertains to different applications than its counterpart. While the MODE-WRELAX algorithm aims at separating overlapping pulses, the MODE-type algorithm was originally developed for parameter estimation of sinusoidal modes. Although the MODE-type algorithm model is slightly different, a minor modification allows it to operate in the same manner as the MODE-WRELAX algorithm, but with the dispersive signal model in (4-60).

The remainder of the section presents the derivation of the algorithm in detail, with necessary adjustments toward our superimposed signal decomposition application (Section 4.6.1). The derivation follows the implementation of the algorithm as suggested earlier [26] (Section 4.6.2). The performance of the algorithm is presented briefly in Section 4.6.3.

4.6.1 Derivation

Cedervall *et al.* [26] presented the MODE-type algorithm based on the following time-domain model

$$\tilde{y}_t = \sum_{l=1}^{L} a_l \rho_l^t + \tilde{e}_t \tag{4-67}$$

where $\tilde{y}_t$ consists of superimposed mixed-mode sinusoids, t is the time sample index, and e_t is zero-mean white noise. This model is almost identical to our model in (4-60) if written in the discrete Fourier domain (replacing *t* with *k*) and letting

$$\begin{aligned} \tilde{Y}_k &= \frac{Y_k}{S_k} \\ \tilde{E}_k &= \frac{E_k}{S_k} \end{aligned} \tag{4-68}$$

However, dividing by the reference spectrum may introduce some problems [25]:

- Possible division by zero (or a very small number);
- Noise is no longer white (assumed by the algorithm);
- Lowering of SNR.

The MODE-WRELAX algorithm successfully circumvented the division altogether, by manipulation of the matrix equations. Rather than re-deriving the MODE-type algorithm to avoid the division, we simply select a valid frequency range where the reference has sufficient energy and thus mitigate the noise issues, at least for the time being. Thus, the revised model is

$$\tilde{Y}_k = \frac{Y_k}{S_k} = \sum_{l=1}^{L} a_l \rho_l^k + \tilde{E}_k \tag{4-69}$$

First, (4-69) is manipulated to resemble the model often used in sensor array signal processing (which is what the original MODE algorithm [21], [22] was developed for). Define the following matrices:

$$\mathbf{y}_k = \begin{bmatrix} \tilde{Y}_k & \cdots & \tilde{Y}_{k+m-1} \end{bmatrix}^T, \tag{4-70}$$

$$\tilde{\mathbf{P}} = \begin{bmatrix} 1 & 1 & \cdots & 1 \\ \rho_1 & \rho_2 & \cdots & \rho_L \\ \vdots & \vdots & & \vdots \\ \rho_1^{m-1} & \rho_2^{m-1} & \cdots & \rho_L^{m-1} \end{bmatrix}, \tag{4-71}$$

$$\mathbf{x}_k = \begin{bmatrix} a_1 \rho_1^k & \cdots & a_L \rho_L^k \end{bmatrix}^T, \tag{4-72}$$

and

$$\mathbf{e}_k = \begin{bmatrix} \tilde{E}_k & \cdots & \tilde{E}_{k+m-1} \end{bmatrix}^T \tag{4-73}$$

for some arbitrary snapshot size $L < m < \tilde{N}$ where $\tilde{N} \le N$ is the number of contiguous DFT samples used in the algorithm. With the above definitions, (4-69) is re-written as

$$\mathbf{y}_k = \widetilde{\mathbf{P}}\mathbf{x}_k + \mathbf{e}_k \tag{4-74}$$

This form corresponds to the sensor array processing form. The following covariance matrix is formed

$$\hat{\mathbf{R}}_d = \sum_{k=1}^{M} \mathbf{y}_{(k-1)d+1}\mathbf{y}_{(k-1)d+1}^H \tag{4-75}$$

where $d > 0$ controls the number of overlapping samples in adjacent snapshots, and M is the total number of snapshots defined as

$$M = \left\lfloor \frac{\widetilde{N} - m}{d} \right\rfloor + 1 \tag{4-76}$$

The operator $\lfloor \cdot \rfloor$ denotes rounding to the nearest smaller or equal integer. Reference [26] contains an example to determine the optimal snapshot size m and the amount of overlap in samples. We have defined a default configuration along the lines of the example where $d = 1$ and $m = 2\hat{L}$, where $\hat{L}$ is the estimated number of signal components.

Assuming large SNR, $\hat{\mathbf{R}}_d$ in (4-75) is close to the true correlation matrix

$$\mathbf{R}_d = \widetilde{\mathbf{P}}\mathbf{G}_d\widetilde{\mathbf{P}}^H \tag{4-77}$$

where

$$\mathbf{G}_d = \sum_{k=1}^{M} \mathbf{x}_{(k-1)d+1}\mathbf{x}_{(k-1)d+1}^H \tag{4-78}$$

Also, let's define the eigenvalue decomposition of $\mathbf{R}_d$ as

$$\mathbf{R}_d = \begin{bmatrix} \mathbf{\Sigma} & \mathbf{G} \end{bmatrix} \begin{bmatrix} \mathbf{\Lambda} & \mathbf{0} \\ \mathbf{0} & \mathbf{0} \end{bmatrix} \begin{bmatrix} \mathbf{\Sigma}^H \\ \mathbf{G}^H \end{bmatrix} = \mathbf{\Sigma}\mathbf{\Lambda}\mathbf{\Sigma}^H \tag{4-79}$$

where $\mathbf{\Sigma}$ corresponds to the L principal eigenvectors and $\mathbf{\Lambda}$ to the diagonal matrix with the corresponding principal eigenvalues on its diagonal. $\mathbf{G}$ corresponds to the eigenvectors that span the signal-free space. By equating (4-77) and (4-79), it is readily shown that the range spaces of $\mathbf{A}$ and $\mathbf{\Sigma}$ are the same.

Analogous to the MODE algorithm, define an L-th order polynomial

$$B(z) = \sum_{k=0}^{L} b_k z^k = b_L \prod_{k=1}^{L} (z - \rho_k) \tag{4-80}$$

and let

$$\mathbf{B}^H = \begin{bmatrix} b_0 & \cdots & b_L & & 0 \\ & \ddots & & \ddots & \\ 0 & & b_0 & \cdots & b_L \end{bmatrix}_{(m-L)\times m} \tag{4-81}$$

The matrices $\mathbf{B}$ and $\tilde{\mathbf{P}}$ are orthogonal, *i.e.*,

$$\mathbf{B}^H \tilde{\mathbf{P}} = \mathbf{0} \tag{4-82}$$

The derivation for the above condition is the same as the derivation for the orthogonality condition in (4-28). The Vandermonde matrix $\mathbf{E}$ in (4-28) is the constrained version of $\tilde{\mathbf{P}}$ with all its elements on the unit circle.

Since both $\mathbf{A}$ and $\mathbf{\Sigma}$ share the same range space, (4-82) can be rewritten as

$$\mathbf{B}^H \mathbf{\Sigma} = \mathbf{0} \tag{4-83}$$

Let $\hat{\mathbf{\Sigma}}$ and $\hat{\mathbf{\Lambda}}$ denote the sample counterparts of $\mathbf{\Sigma}$ and $\mathbf{\Lambda}$. Then we are interested in finding the $\hat{B}(z)$ polynomial — an estimate of $B(z)$ — such that

$$\hat{\mathbf{B}}^H \hat{\mathbf{\Sigma}} \simeq \mathbf{0} \tag{4-84}$$

Such $B(z)$ can be found by minimizing the quadratic cost function

$$\begin{aligned} f(\mathbf{b}) &= \mathrm{tr}\left[\left(\mathbf{W}_1^{1/2}\mathbf{B}^H\hat{\mathbf{\Sigma}}\mathbf{W}_2^{1/2}\right)\left(\mathbf{W}_1^{1/2}\mathbf{B}^H\hat{\mathbf{\Sigma}}\mathbf{W}_2^{1/2}\right)^H\right] \\ &= \mathrm{tr}\left[\left(\mathbf{B}\mathbf{W}_1\mathbf{B}^H\hat{\mathbf{\Sigma}}\mathbf{W}_2\hat{\mathbf{\Sigma}}^H\right)\right] \end{aligned} \tag{4-85}$$

over

$$\mathbf{b} = \begin{bmatrix} b_0 & \cdots & b_L \end{bmatrix} \tag{4-86}$$

The weighting matrices suggested by Cedervall *et al.* are $\mathbf{W}_2 = \mathbf{\Lambda}$ and $\mathbf{W}_1 = \left(\mathbf{B}^H\mathbf{B}\right)^{-1}$ [26].

4.6.2 Implementation

Cedervall *et al.* [26] also outlines the implementation for finding the minimizer for the expression in (4-85). The proposed method is outlined in Figure 4-19. The process includes two consecutive evaluations of the cost function

$$f_W(\mathbf{b}) = \mathrm{tr}\left[\mathbf{B}\mathbf{W}\mathbf{B}^H\hat{\mathbf{\Sigma}}\hat{\mathbf{\Lambda}}\hat{\mathbf{\Sigma}}^H\right] \tag{4-87}$$

with the weighting matrix **W** specified differently for each evaluation.

1. Compute the L principal eigenpairs of $\hat{\mathbf{R}}_d$ for a given *m* and *d*.
2. Estimate $\hat{\mathbf{b}}$ such that (4-87) is minimized from an initial guess for **B** and with $\mathbf{W} = \mathbf{I}$.
3. Enhance the estimate by reevaluating (4-87) with $\hat{\mathbf{B}}$, based on $\hat{\mathbf{b}}$, and $\mathbf{W} = \left(\hat{\mathbf{B}}^H\hat{\mathbf{B}}\right)^{-1}$.
4. Obtain $\{\hat{\rho}_k\}$ from $\{\hat{b}_k\}$ (roots of the polynomial $\hat{B}(z)$).

Figure 4-19: Outline of the MODE-type algorithm procedure [26].

There is an efficient implementation to minimize (4-87) utilizing matrix vectorization and Kronecker (tensor) product techniques. First, based on the property of trace operation, the cost function is rewritten as follows:

$$f_W(\mathbf{b}) = \mathrm{tr}\left[\mathbf{B}^H\hat{\mathbf{\Sigma}}\hat{\mathbf{\Lambda}}\hat{\mathbf{\Sigma}}^H\mathbf{B}\mathbf{W}\right] \tag{4-88}$$

Replacing the trace operator with a summation operator yields

$$f_W(\mathbf{b}) = \sum_{i=1}^{m-L} \mathbf{b}_{\bullet i}^H \hat{\mathbf{\Sigma}} \hat{\mathbf{\Lambda}} \hat{\mathbf{\Sigma}}^H \mathbf{B} \mathbf{w}_{\bullet i} \tag{4-89}$$

where $\mathbf{b}_{\bullet i}$ and $\mathbf{w}_{\bullet i}$ are *i*-th column vectors of $\mathbf{B}$ and $\mathbf{W}$, respectively. The remaining $\mathbf{B}$ matrix can also be decomposed into a sum of its column vectors as follows

$$f_W(\mathbf{b}) = \sum_{i=1}^{m-L} \mathbf{b}_{\bullet i}^H \sum_{j=1}^{m-L} w_{ji} \hat{\mathbf{\Sigma}} \hat{\mathbf{\Lambda}} \hat{\mathbf{\Sigma}}^H \mathbf{b}_{\bullet j} \tag{4-90}$$

where w_{ji} is the *ji*-th element of $\mathbf{W}$. Let

$$\widetilde{\mathbf{b}} = \mathrm{vec}(\mathbf{B}) = \begin{bmatrix} \mathbf{b}^T & 0^T & \mathbf{b}^T & 0^T & \cdots \end{bmatrix}^T \tag{4-91}$$

with **vec** denoting the vectorization operator; then (4-90) becomes

$$f_W(\mathbf{b}) = \widetilde{\mathbf{b}}^H \begin{bmatrix} w_{11} \hat{\mathbf{\Sigma}} \hat{\mathbf{\Lambda}} \hat{\mathbf{\Sigma}}^H & \cdots & w_{(m-L)1} \hat{\mathbf{\Sigma}} \hat{\mathbf{\Lambda}} \hat{\mathbf{\Sigma}}^H \\ \vdots & & \vdots \\ w_{1(m-L)} \hat{\mathbf{\Sigma}} \hat{\mathbf{\Lambda}} \hat{\mathbf{\Sigma}}^H & \cdots & w_{(m-L)(m-L)} \hat{\mathbf{\Sigma}} \hat{\mathbf{\Lambda}} \hat{\mathbf{\Sigma}}^H \end{bmatrix} \widetilde{\mathbf{b}} \tag{4-92}$$

The matrix expression in (4-92) is a Kronecker (or tensor) product of $\mathbf{W}^T$ and $\hat{\mathbf{\Sigma}} \mathbf{\Lambda} \hat{\mathbf{\Sigma}}^H$. Therefore, (4-92) can be denoted as follows

$$f_W(\mathbf{b}) = \widetilde{\mathbf{b}}^H \left(\mathbf{W}^T \otimes \hat{\mathbf{\Sigma}} \mathbf{\Lambda} \hat{\mathbf{\Sigma}}^H \right) \widetilde{\mathbf{b}} \tag{4-93}$$

where $\otimes$ denotes the Kronecker product operator. Define $\overline{\mathbf{\Omega}}$ to be the matrix $\mathbf{W}^T \otimes \hat{\mathbf{\Sigma}} \mathbf{\Lambda} \hat{\mathbf{\Sigma}}^H$ from which the rows and columns corresponding to the zeros in $\widetilde{\mathbf{b}}$ are eliminated. Let

$$\mathbf{\Omega} = \begin{bmatrix} \mathbf{I} & \cdots & \mathbf{I} \end{bmatrix} \overline{\mathbf{\Omega}} \begin{bmatrix} \mathbf{I} \\ \vdots \\ \mathbf{I} \end{bmatrix} \tag{4-94}$$

then (4-87) can finally be expressed as

$$f_W(\mathbf{b}) = \mathbf{b}^H \mathbf{\Omega b} \tag{4-95}$$

For a fixed norm of **b**, the quadratic cost function in (4-95) is minimized by selecting the smallest eigenvector of $\mathbf{\Omega}$. Note that the initial evaluation of (4-95) (Step 2 in Figure 4-19) is now independent of **B** (*i.e.* no initial guess required). Once $\hat{B}(z)$ is determined, both $\hat{\boldsymbol{\varrho}}$ and $\hat{\mathbf{a}}$ are readily obtained.

4.6.3 Algorithm Performance with Known Signal

To verify the proper operation of the MODE-type algorithm, the algorithm is tested with three known signals. The first test is in the sinusoidal parameter estimation context, which is what the MODE-type algorithm was originally proposed for. The second and third tests parallel the test carried out for MODE-WRELAX in Section 1.4, for decomposing superimposed pulses. The pulses are now dispersed according to the MODE-type signal model.

The first test is the identification of the poles associated with the sum of 10 random sinusoids with various modes. Each sinusoid is normalized to have the same energy (over the measured frequency samples) as any other sinusoid. Figure 4-20 shows the sum of the sinusoids, while Figure 4-21 illustrates the location of the poles ('x' marks). The pole estimates obtained by the MODE-type algorithm are shown in Figure 4-22 under two different environments. Figure 4-22(a) is the result when there is no noise (SNR = ∞) added to the signal in Figure 4-20. As clearly illustrated in the figure, the true poles are accurately estimated (the red •'s are precisely on the blue x's). Figure 4-22(b), on the other hand, shows the Monte Carlo simulation result of estimating poles in additive white noise for an SNR of 20 dB. While some variations are observed, all poles are consistently found by the MODE-type algorithm.

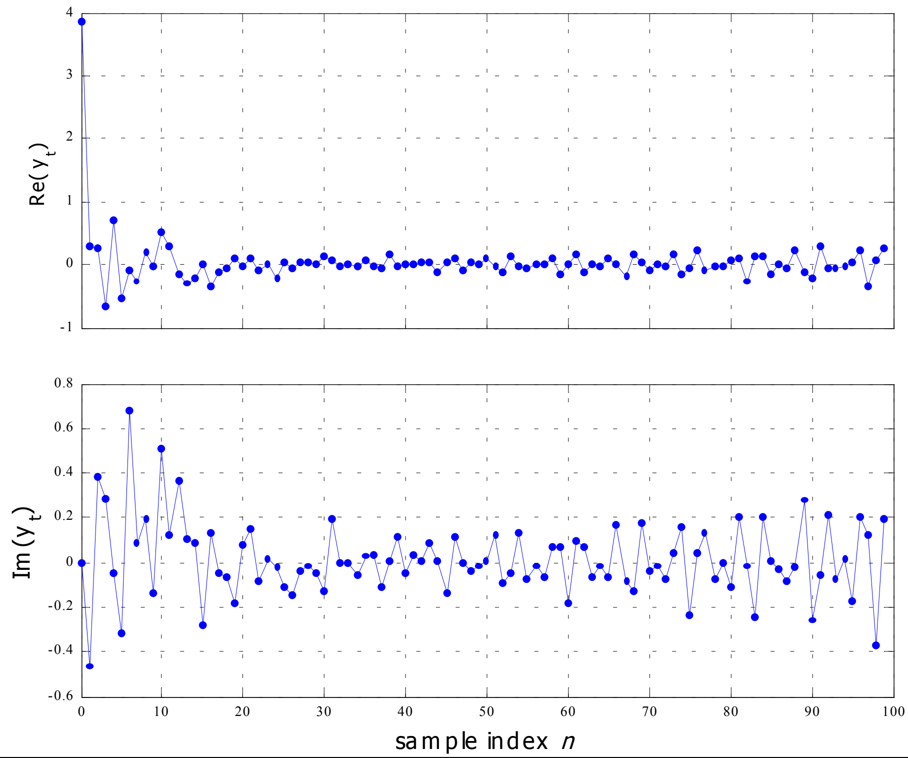

Figure 4-20: Signal for MODE-type test 1 — Sum of 10 exponential modes.

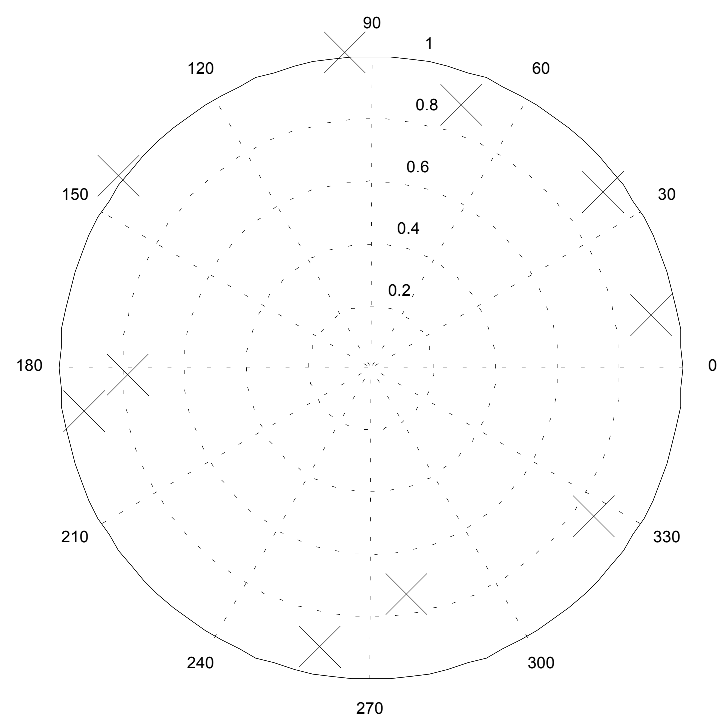

Figure 4-21: Pole location of ten sinusoidal modes.

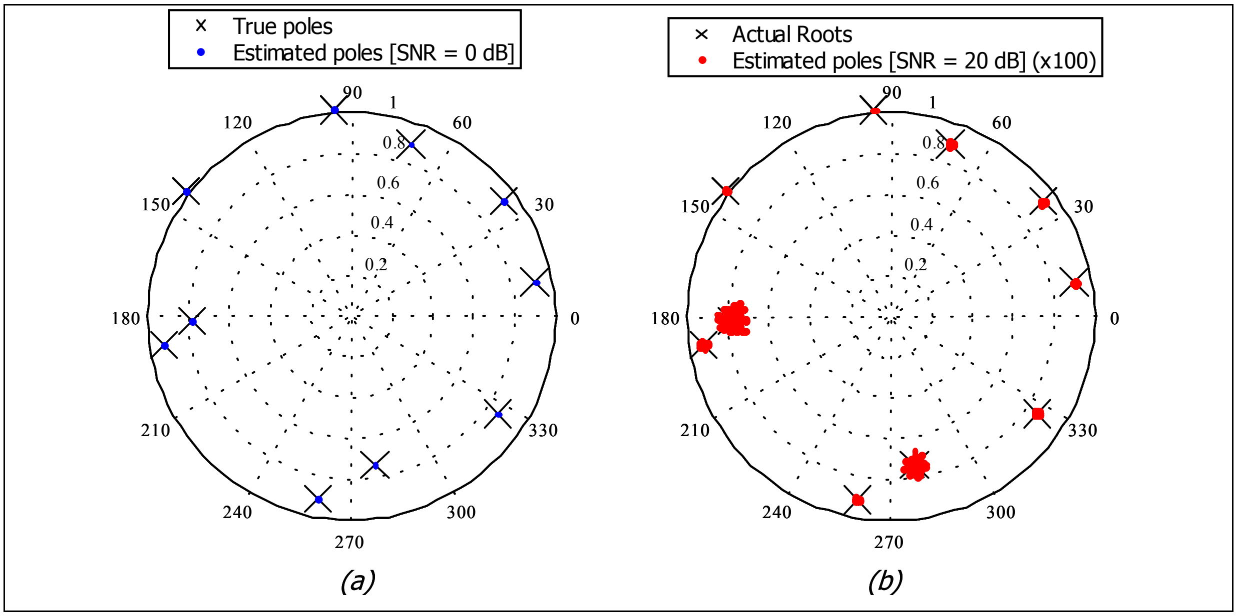

Figure 4-22: Estimation results — SNR = 0 dB (a) and SNR = 20 dB (b).

The next two experiments demonstrate the ability of the MODE-type algorithm in decomposition of overlapping pulses by applying it to arbitrary – but known – pulses. The MODE-type algorithm is compared to the MODE (without WRELAX stage) and MODE-WRELAX algorithms with an objective signal that is the superimposition of scaled, delayed, and dispersed versions of a reference pulse. Two experiments are carried out: with objective pulses that are either well-spaced or substantially overlapping. Let us again consider the discrete raised-cosine reference pulse, which was used for the MODE-WRELAX test in Section 4.3.3,

$$s_n = \begin{cases} 0.5(1-\cos 0.1\pi n), & 0 \le n < 20 \\ 0, & \text{elsewhere} \end{cases} \tag{4-96}$$

The pulse width is twice as wide as the previous one, in (4-57). The waveform over $n = 0:500$ is shown in Figure 4-23(a). Its 512-point DFT magnitude spectrum is also shown in Figure 4-23(b) (only for positive frequencies shown).

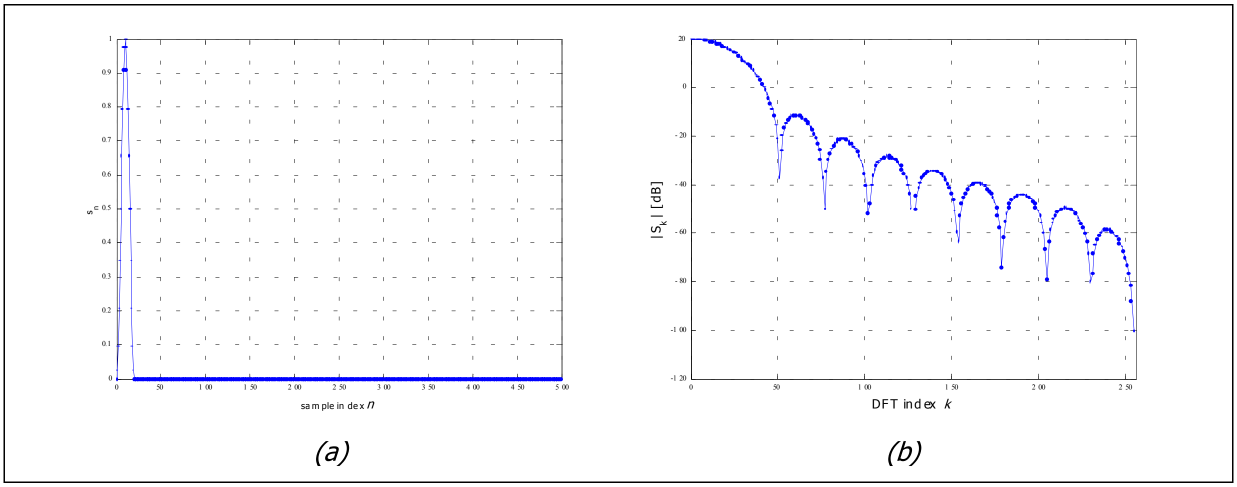

Figure 4-23: Reference raised-cosine pulse (a) and its 512-point DFT magnitude spectrum in dB (b). (only positive frequency shown)

First, the combination of three visually separable (i.e. well-spaced) pulses is considered. To construct the composite of overlapping pulses, based on the given reference pulse, we arbitrarily selected L = 3, $\mathbf{a} = \begin{bmatrix}1 & 0.95 & 0.54\end{bmatrix}$, $\boldsymbol{\tau} = \begin{bmatrix}97.4 & 184.6 & 217.9\end{bmatrix}$, and $\boldsymbol{\zeta} = \begin{bmatrix}1 & 0.5 & 0.3\end{bmatrix}$. Figure 4-26(a) illustrates the individual pulses. The resulting linear combination y(t) is shown in Figure 4-26(b). The Figure 4-26(b) waveform is generated based on its 512-point evenly-spaced frequency spectrum samples by evaluating (4-60) with the DFT of the reference signal (Figure 4-23(a)) and the signal parameters defined above, as well as assuming a noiseless environment, *i.e.* $E_k = 0$. Note that, since the input waveform is already in the discrete-time domain, the sampling frequency f_s is set to 1. The discrete time-domain signal is obtained by taking the inverse DFT of the frequency samples (note that only samples for $n = 0:500$ are displayed in the figure).

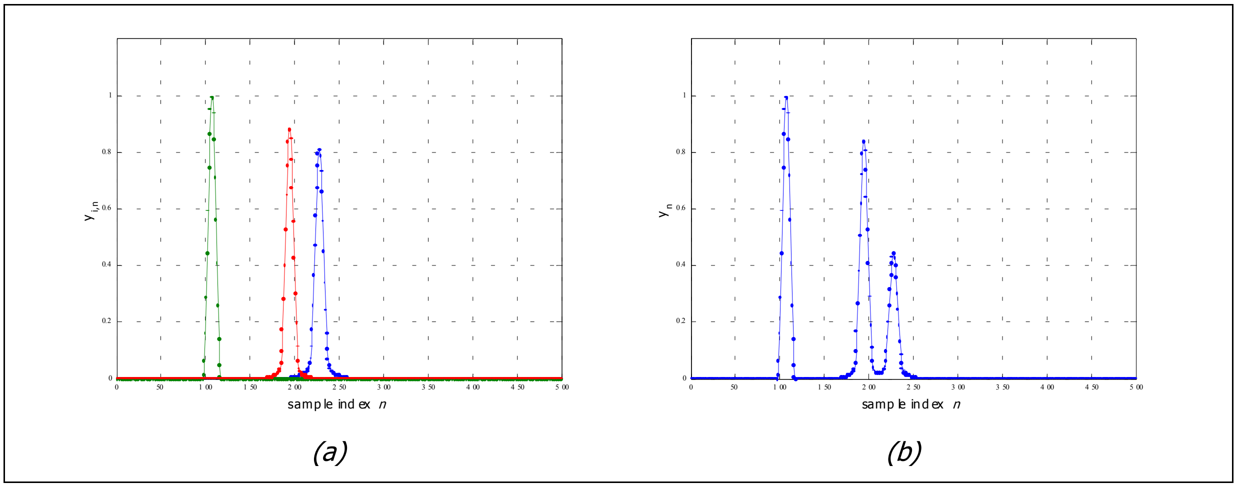

Figure 4-24: MODE-type test signal 1 with sparsely overlapping pulses; individual pulses (a), combined signal (b).

To avoid estimation errors caused by possible aliasing — even at very small magnitudes — the frequency samples are directly fed to the estimation algorithms, instead of applying a series of inverse and forward DFTs. Under the assumption that we know the number of constituent pulses (*i.e.* $\hat{L} = 3$), the estimation results of the MODE, MODE-WRELAX, and MODE-type algorithms, are presented in Table 4-7; moreover, reconstructed signals are displayed in Figure 4-25 The algorithms utilize only the 41 frequency samples over $k = 0:40$, from the 512-point DFT samples S_k and Y_k. Again the frequency range is determined by where the reference signal power is concentrated (for our reference signal that is in the low frequency region) to avoid division by a small quantity.

Table 4-7: MODE-type experiment 5-1 — parameter estimation results for $\hat{L} = 3$. (Best estimates highlighted)

Signal component		True Solution	Algorithm		
			MODE only	**MODE-WRELAX**	**MODE-type**
$\hat{Y}_{1,n}$	τ_1	97.4	97.4	97.327	97.4
	ζ_1	1	*(1)*	*(1)*	1
	$\mathrm{Re}\{a_1\}$	1.00	1.005	1.0054	1
	$\mathrm{Im}\{a_1\}$	0	–0.0057788	–0.016372	0
$\hat{Y}_{2,n}$	τ_2	184.6	184.6	184.43	184.6
	ζ_2	0.5	*(1)*	*(1)*	0.5
	$\mathrm{Re}\{a_2\}$	0.95	0.86667	0.86325	0.95
	$\mathrm{Im}\{a_2\}$	0	–0.009673	–0.03071	0
$\hat{Y}_{3,n}$	τ_3	217.9	217.9	218.25	217.9
	ζ_3	0.3	*(1)*	*(1)*	0.3
	$\mathrm{Re}\{a_3\}$	0.54	0.4625	0.45905	0.54
	$\mathrm{Im}\{a_3\}$	0	0.010316	0.03288	0

All three algorithms identified the pulse without dispersion (the pulse near n = 100) fairly accurately (the dispersed pulses somewhat affected the precision of the original algorithms). As clearly shown with the other two dispersed pulses, the MODE-type algorithm detects the dispersed pulses more accurately. It is interesting to note that the MODE algorithm alone accurately estimates all the delays while it compensates for its incompatibility with dispersion by using a complex scaling factor, and the WRELAX algorithm displaces these pulses from the initially correct delays to further compensate for the dispersion. However, the superiority of the MODE-type algorithm is particularly apparent when the overlapping pulses are reconstructed based on the corresponding model and compared to the original signal, as shown in Figure 4-25.

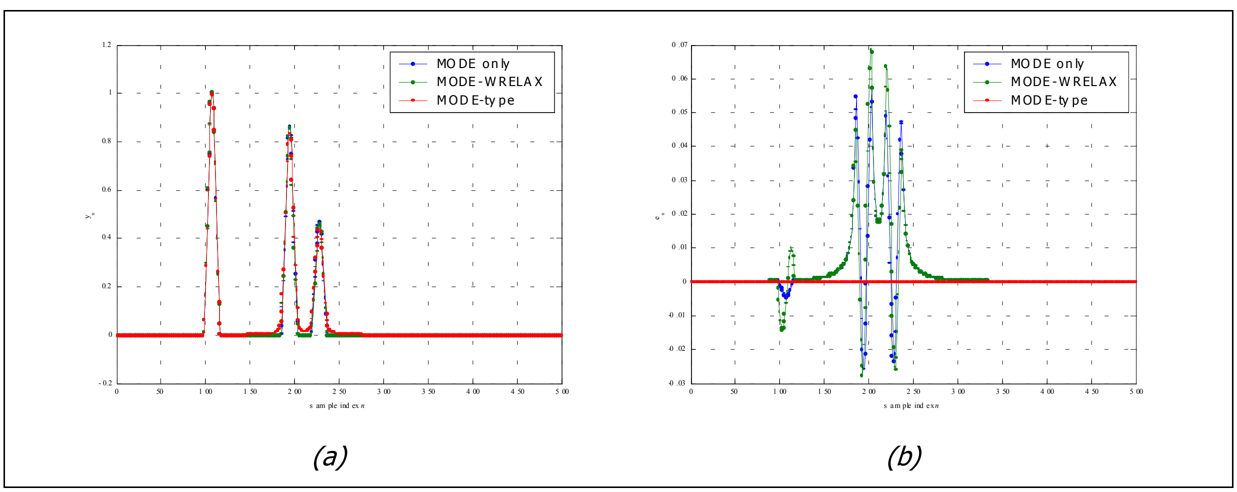

Figure 4-25: MODE-type experiment 2 — reconstructed objective signal with MODE, MODE-WRELAX, and MODE-type algorithms (a) and corresponding estimation errors (b).

The second experiment uses the same raised cosine reference pulse, as shown in Figure 4-23(a), but the objective pulses are now substantially overlapping. The exact same L, $\mathbf{a}$, and $\boldsymbol{\zeta}$ from the previous experiment are used, while the delays are changed to $\boldsymbol{\tau} = \begin{bmatrix} 99.5 & 100.0 & 104.9 \end{bmatrix}$. The resulting objective pulses (before combining) and the superimposed signal are shown in Figures 4-26(a) and 4-26(b), respectively.

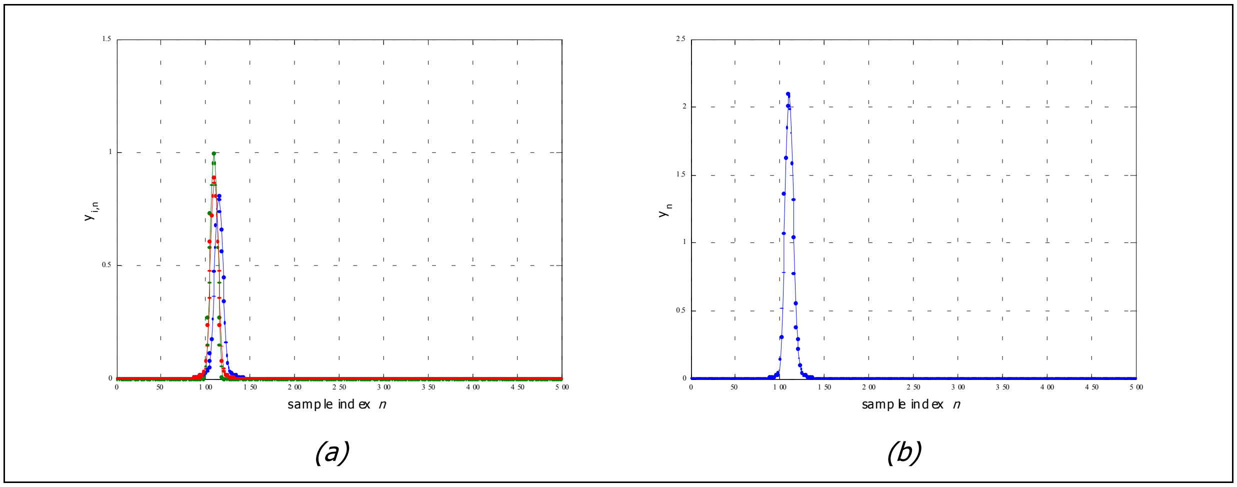

Figure 4-26: MODE-type test signal 2 with substantially overlapping pulses; individual pulses (a), combined signal (b).

The procedure used in the previous experiment is used here too. With the correct number of pulses given, the estimation results for each algorithm are tabulated in Table 4-8; the reconstructed signals, based on the parameter estimates for the three algorithms, are shown in Figure 4-27.

Table 4-8: Experiment 5-1 — parameter estimation results with $\hat{L} = 3$ (best estimates highlighted).

Signal component		True Solution	Algorithm		
			MODE only	**MODE-WRELAX**	**MODE-type**
$\hat{Y}_{1,n}$	τ_1	99.5	99.495	99.495	99.497
	ζ_1	1	*(1)*	*(1)*	0.99663
	$\mathrm{Re}\{a_1\}$	1.00	0.034858	0.03489	1.0031
	$\mathrm{Im}\{a_1\}$	0	0.8111	0.81113	0.011456
$\hat{Y}_{2,n}$	τ_2	100.0	99.993	99.993	99.995
	ζ_2	0.5	*(1)*	*(1)*	0.49761
	$\mathrm{Re}\{a_2\}$	0.95	2.0462	2.0462	0.94676
	$\mathrm{Im}\{a_2\}$	0	–0.61124	–0.61121	0.011414
$\hat{Y}_{3,n}$	τ_3	104.9	104.9	104.9	104.9
	ζ_3	0.3	*(1)*	*(1)*	0.29995
	$\mathrm{Re}\{a_3\}$	0.54	0.41115	0.41111	0.54012
	$\mathrm{Im}\{a_3\}$	0	–0.20497	–0.20505	0

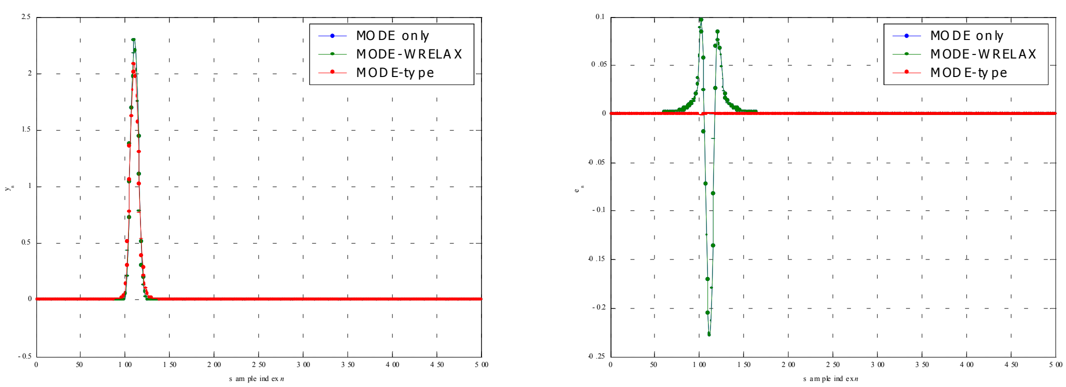

(a) *(b)*

Figure 4-27: MODE-type experiment 1— reconstructed objective signal with MODE, MODE-WRELAX, and MODE-type algorithms (a) and corresponding estimation errors (b). (MODE-WRELAX on top of MODE)

Evidently, the reconstruction results in Figure 4-27 show both overall accuracy and accurate individual pulse detection capability of the MODE-type algorithms. However, while MODE and MODE-WRELAX failed to reconstruct the individual pulses overall (in terms of amplitude and delay), its delay approximations itself were rather good and comparable to the estimates from the MODE-type algorithm. This is perhaps due to the additional parameters being estimated in the MODE-type algorithm; an increase in the number of estimated parameters causes an increase in the error variance of the individual estimates.

4.7 Application of Mode-Type Algorithm in TDR Reflection Decomposition

The procedure to apply the MODE-type algorithm is essentially the same as for the MODE-WRELAX algorithm in Section 4.4. The experiment in Section 4.4 is repeated with the MODE-type algorithm in this section as well as the CSA #1 case study from Chapter 3. In Section 4.5, we determined? that the frequency range from 1 MHz to 2 MHz allows a good match between the TP characteristics and the MODE-type signal model. With the 2^{15}-point DFT and the sampling frequency of 40 MHz used in the Section 4.4 experiment, the equivalent frequency sample indices are k = 820:1638. Since the MODE-type algorithm does not require such a large number of data samples, only every eighth DFT value is used in the algorithm. With reference and overlapping spectra as shown in Figure 4-11 and for the number of reflections estimated at $\hat{L}$= 2:7 each, the MODE-type algorithm is applied and the resulting estimates listed in Table 4-9. When the results in this table are compared to those in Table 4-5, for MODE-WRELAX estimates, it is apparent that the MODE-type algorithm has captured more reflections than the MODE-WRELAX algorithm. The reflection at n = 20, previously unidentified, appears in the MODE-type estimates. However, the behavior of each detected mode is rather peculiar. The ζ_i indicates that most estimated reflections are explosive ($\zeta_i > 1$) while we have observed that later reflections are more dispersed (*e.g.*, damped). Moreover, for a high number of estimated reflections, the amplitude parameter fails (a numerical issue). Despite these remaining concerns, the MODE-type algorithm seems to detect overlapping TDR reflections more accurately than the MODE-WRELAX algorithm, particularly in terms of their TOAs.

Table 4-9: MODE-type estimates for TDR decomposition.

$\hat{L}$	$y_{i,n}$	τ_i	ζ_i	$\lvert a_i \rvert$	$\angle a_i$
2	$y_{1,n}$	9.39	1.0021	0.0093367	-1.9381
	$y_{2,n}$	31.65	1.0058	1.4614e-005	-1.8384
3	$y_{1,n}$	7.9238	1.002	0.012003	0.81257
	$y_{2,n}$	26.472	1.0039	0.00023023	-2.2548
	$y_{3,n}$	119.67	0.99672	0.23252	-2.4275
4	$y_{1,n}$	7.3014	1.0017	0.017693	-0.80865
	$y_{2,n}$	25.071	1.0034	0.00048523	0.35442
	$y_{3,n}$	89.081	0.99698	0.27272	-2.8667
	$y_{4,n}$	127.28	1.0027	0.00029177	0.019621
5	$y_{1,n}$	6.4441	1.0018	0.020384	-3.0811
	$y_{2,n}$	22.602	1.0036	0.00048616	0.56586
	$y_{3,n}$	55.576	1.0032	0.00029362	2.0507
	$y_{4,n}$	123.49	1.0018	0.0010215	-3.1253
	$y_{5,n}$	906.95	0.96634	–	–
6	$y_{1,n}$	6.0188	1.0013	0.040292	2.0039
	$y_{2,n}$	21.449	1.0029	0.0013684	-2.4841
	$y_{3,n}$	49.679	1.0048	3.9883e-005	-0.29194
	$y_{4,n}$	121.18	1	0.0050212	-1.7755
	$y_{5,n}$	224.62	0.97014	–	–
	$y_{6,n}$	1002.5	0.87765	–	–
7	$y_{1,n}$	5.719	1.0013	–	–
	$y_{2,n}$	20.689	1.003	–	–
	$y_{3,n}$	47.293	1.0071	–	–
	$y_{4,n}$	118.7	1.0008	–	–
	$y_{5,n}$	174.93	1.0128	–	–
	$y_{6,n}$	957.56	1.0514	–	–
	$y_{7,n}$	3510.5	0.00074755	2.0378×10^{-5}	3510.9

4.8 Summary

This chapter has introduced two types of MODE-based algorithm in an attempt to resolve overlapping TDR reflections. The MODE-WRELAX algorithm, developed for a similar application, was implemented first. However, we discovered that the signal model (linear combination of the same, delayed and scaled pulses) associated with the MODE-WRELAX algorithm does not apply to the TDR reflections due to the dispersive nature of the TP medium. To accommodate the dispersion, another algorithm, the MODE-type algorithm — which was originally developed for sinusoidal parameter estimation — was presented next. The signal model for the MODE-type algorithm incorporates dispersive behavior that is relatively compatible with that of TDR reflections, and the

MODE-type algorithm has shown some promise for TDR reflection decomposition. If applied properly, the MODE-type algorithm can contribute significantly to the TP loop identification process, especially with close segments present.

Incorporation of the MODE-type algorithm into the TDR-based identification process is the apparent next step. However, the extensive study of the algorithm for decomposing TDR responses has lead to another approach to TP loop identification in which the MODE-type algorithm would be more fully utilized. Both MODE algorithms operate in the Fourier domain (for our application) and to apply them the DFT of the TDR response must be computed. This, in addition to the typically long data length, can be relatively time consuming and inefficient. The alternative approach is to start with frequency domain data, or the frequency response of the loops. The subsequent chapter combines the ability of the MODE-type algorithm to accurately estimate the TOA of reflections with the iterative modeling approach developed in the time-domain approach to perform the loop identification with the frequency-response measurement data.